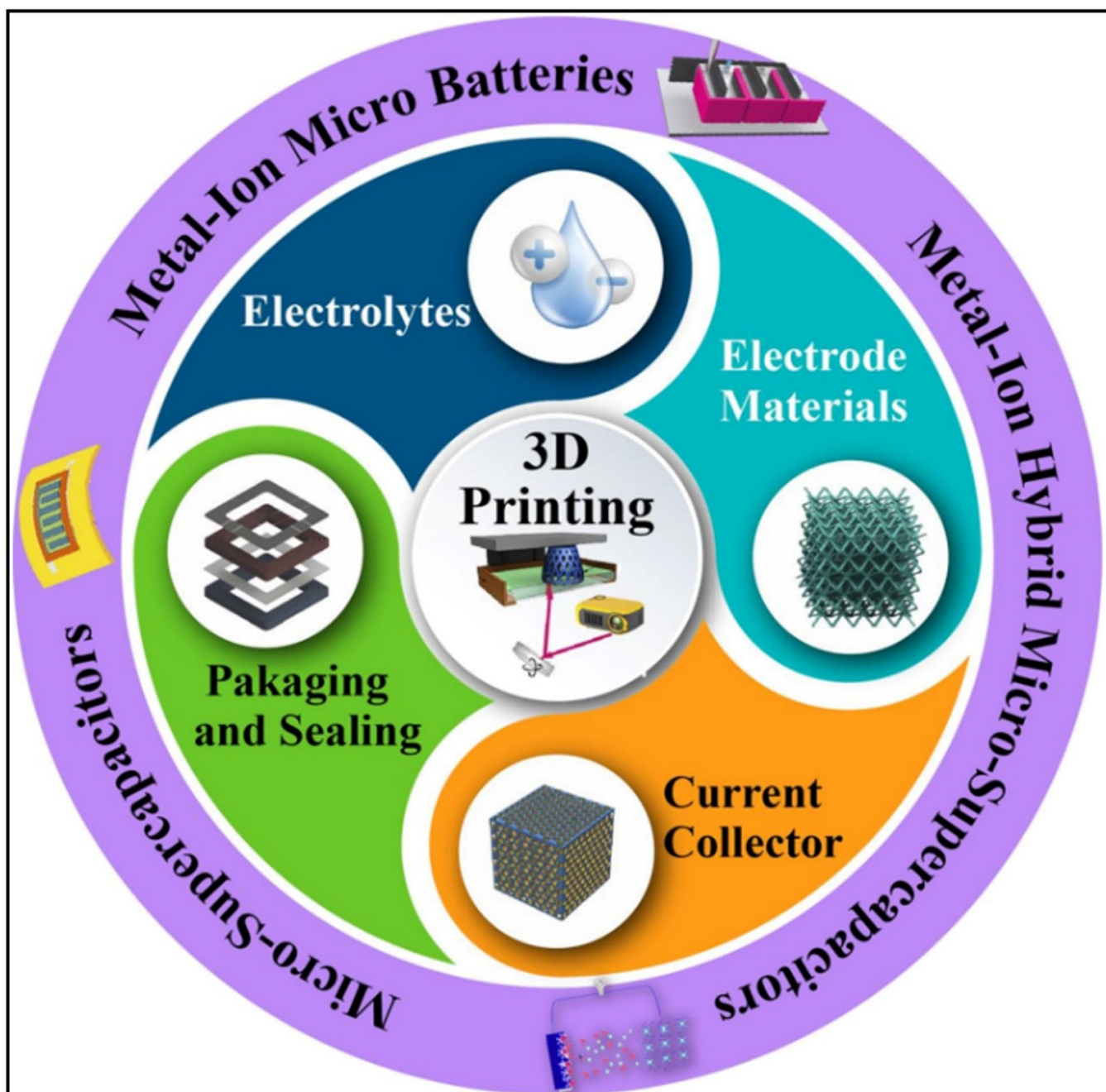


# 3D Printed Micro-Electrochemical Energy Storage Devices

Abdul Jabbar Khan<sup>+</sup>,<sup>[a]</sup> Abdul Mateen<sup>+</sup>,<sup>[b]</sup> Shaukat Khan,<sup>[c]</sup> Liang He,<sup>[d]</sup> Wenwu Wang,<sup>[d]</sup> Arshid Numan,<sup>[e]</sup> Kui-Qing Peng,<sup>[b]</sup> Iftikhar Ahmed Malik,<sup>[f]</sup> Ijaz Hussain,<sup>[g]</sup> and Guowei Zhao\*<sup>[a]</sup>



Micro-electrochemical energy storage devices (MEESDs) including micro-supercapacitors (MSCs), micro-batteries (MBs), and metal-ion hybrid micro-supercapacitors (MIHMSCs) are critical components of electronic systems, especially in the expanding field of the Internet of Things (IoT). In recent years, three-dimensional (3D) printing techniques also known as additive manufacturing (AM) techniques have emerged as promising approaches to overcome the limitations of conventional fabrication procedures. Employing advanced manufacturing techniques to fabricate MEESDs offers potential benefits, including mass production and programmable prototyping. In this review, we provide a comprehensive overview of the recent advancements in the applications of 3D printing techniques for MEESDs such as MBs, MSCs, and MIHMSCs. First, this review

discusses the fundamental of micro/nano energy storage devices by 3D printing technology. Further, we examine the critical properties of the printable inks used in these processes. We also highlighted the current developments in 3D printing-based MEESDs including various types of MBs, pseudocapacitive and electrochemical double-layer-based MSCs, and a range of MIHMSCs. Additionally, this review addresses the challenges and future prospects of 3D printing based MEESDs, including material limitations, printing resolution, manufacturing scalability, mechanical properties, and cost. Overall, this review presents a unique and valuable contribution by providing a comprehensive overview of the recent advancements in 3D printing based MEESDs.

## 1. Introduction

Micro-electrochemical energy storage devices (MEESDs) specifically designed for the storage and delivery of electrical power, have found widespread applications. These devices serve not only as a power source for portable electronic devices and vehicles but also play a crucial role in renewable energy systems and power grids.<sup>[1]</sup> The development of MEESDs has become a critical area of research in recent years. However, the fabrication of these devices has been hindered by the lack of efficient manufacturing techniques.<sup>[2]</sup> Fortunately, three-dimensional (3D) printing technology has emerged as a promising solution to design MEESDs. 3D printing offers the ability to

produce intricate designs and complex geometries that are often challenging or even unachievable with traditional manufacturing methods.<sup>[3,4]</sup> The purpose of this review is to provide a comprehensive overview of the current state-of-the-art 3D-printed MEESD. It explores the diverse range of electrode materials utilized in the production of these devices, along with their performance characteristics and potential applications. Additionally, this review highlights the existing challenges and opportunities in this field and provides recommendations for future research directions.

3D printing technology is helpful in a wide variety of scientific fields due to its advantages such as high speed, low cost, and fabricating complicated structures.<sup>[6]</sup> This technique involves the precise layer-by-layer assembly of structures based on computer-aided design/manufacturing (CAD/CAM) principles, enabling the construction of complex designs by viewing them as the assembly of sliced layers.<sup>[7]</sup> The differences between a variety of printing technologies are depicted in Figure 1. Comparisons between different printing technologies are provided such as taking accuracy, resolution, throughput, surface finish, and other factors. 3D printing can be divided into seven primary categories according to the ISO/ASTM 52900:2015 standard: material extrusion, vat photo-polymerization, powder bed fusion, binder jetting, material jetting, sheet lamination, and directed energy deposition.<sup>[8]</sup> These techniques enable the production of functional structures with programmable structural properties at various length scales, which can be challenging to achieve through traditional manufacturing methods. In particular, 3D printing allows for highly accurate and effective customization of the micro/nano structure and components of printed MEESDs.<sup>[9]</sup> The programmable designing and manufacturing capabilities significantly increase the structural variety and complexity, performance, and usefulness of MEESDs. Additionally, 3D printing's additive nature and the material's precise deposition technique optimize the material's consumption and reduce premature depletion, which is compatible with the promising trend of sustainable MEESDs.<sup>[10]</sup>

3D printing offers the fabrication of objects from a wide variety of materials, including polymers,<sup>[11]</sup> metals,<sup>[12]</sup>

[a] Dr. A. Jabbar Khan,<sup>†</sup> Prof. G. Zhao  
*College of Chemistry and Chemical Engineering  
 Huanggang Normal University  
 Huanggang 438000 (China)*  
*E-mail: zhaoguowei@hgnu.edu.cn*

[b] A. Mateen,<sup>†</sup> Prof. K.-Q. Peng  
*Department of Physics and Beijing Key Laboratory of Energy Conversion and Storage Materials  
 Beijing Normal University  
 Beijing, 100084 (China)*

[c] Dr. S. Khan  
*Department of Chemical Engineering  
 College of Engineering  
 Dhofar University  
 Salalah 211 (Oman)*

[d] Prof. L. He, W. Wang  
*School of Mechanical Engineering  
 Sichuan University  
 Chengdu 610065 (P. R. China)*

[e] Dr. A. Numan  
*Graphene & Advanced 2D Materials Research Group  
 School of Engineering and Technology  
 Sunway University  
 47500 Petaling Jaya, Selangor (Malaysia)*

[f] Dr. I. Ahmed Malik  
*School of Physics and Technology  
 Wuhan University  
 Wuhan 430072 (P.R. China)*

[g] Dr. I. Hussain  
*Center for Refining & Advanced Chemicals  
 King Fahd University of Petroleum & Minerals  
 Dhahran 31261 (Saudi Arabia)*

[†] These authors contributed equally to this paper.

ceramics,<sup>[13]</sup> biomaterials,<sup>[14]</sup> and composites.<sup>[15]</sup> It has found applications in various fields, including electronics,<sup>[16]</sup>

construction,<sup>[17]</sup> biotechnology,<sup>[18]</sup> and electrochemical energy storage.<sup>[19]</sup> Recently, 3D printing has garnered much attention



Dr. Abdul Jabbar Khan is currently serving as an Associate Professor in the College of Chemistry and Chemical Engineering, Huanggang Normal University, China. Mr. Khan earned his MS degree at the Department of Physics from Air University Islamabad, Pakistan, in 2016 and obtained his Ph.D. in Materials and Processing Engineering from the South China University of Technology in 2020. His research interest focuses on metal oxide, carbon, and MXene-based nanomaterials for energy storage devices (supercapacitors and all solid-state lithium-ion batteries).



Mr. Abdul Mateen is currently a Ph.D. candidate at the department of Physics, Beijing Normal University, Beijing China. He received his Master's degree in physics in 2013 from Mirpur University of Science and Technology (MUST), Mirpur, AJK, Pakistan. He completed Master's in philosophy in Solid State Physics in 2015 from University of Punjab, Lahore Pakistan. His research interest focuses on 2D materials (Silicon, MXene, Transition metal oxides, and Metal-organic frameworks) for energy storage devices specifically supercapacitors.



Dr. Shaukat Khan is currently serving as an Assistant Professor in the department of Chemical Engineering, College of Engineering at Dhofar University, Salalah, Oman. Dr. Shaukat Khan obtained his Ph.D. degree from Kyungpook National University, South Korea. His research is mainly focused on nanomaterials (nano-carbons, MXene, Transition metal oxides, Metal-organic frameworks, and perovskites) for energy harvesting and storage applications (organic and perovskite solar cells and supercapacitors and metal-ion batteries).



Liang He is a professor at the School of Mechanical Engineering at Sichuan University. He received his Ph.D. from Tohoku University (Japan) in 2013. His current research interests include the microfabrication and characterization of micro/nano devices, MEMS, and on-chip integrated microsystem.



Mr. Wenwu Wang is working towards his Ph.D. in the School of Mechanical Engineering at Sichuan University. His research interests include micro/nano fabrication and biosensing technology.



Dr. Numan Arshid is an Associate Professor at Graphene and Advanced 2D Materials Research Group (GAMRG), School of Engineering and Technology, Sunway University, Malaysia. His research interests are mainly focused on the development of 2D heterostructure nanomaterials for energy storage and electrochemical sensor applications.



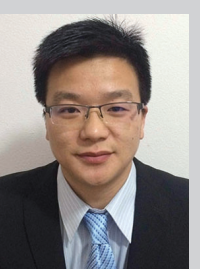
Dr. Kui-Qing Peng received his Ph.D. in Materials Science in 2004 from Tsinghua University, China. He was a senior research staff member from 2004 to 2006 at City University of Hong Kong. He is now a full professor of Materials Physics and Chemistry at Beijing Normal University, China. The development and application of wet etching concepts constitute his major research interests. He is attributed to adopting the metal-catalyzed etching of silicon for the micro/nanofabrication of silicon nanowires and black silicon and made significant contributions to metal-assisted chemical etching (MacEtch) and its emerging applications.



Dr. Iftikhar Ahmed Malik is currently working as a postdoc fellow at the School of Physics and Technology, Wuhan University, China. He obtained his Ph.D. in Condensed Matter Physics from Beijing Normal University, China. His research focuses on the artificial design of oxide-based and 2D materials-based devices for spintronics applications. He focuses on the observation and manipulation of nonlinear spin textures using variable temperature scanning probe microscopy.



Dr. Ijaz Hussain is currently employed as a postdoctoral researcher at King Fahd University of Petroleum & Minerals (KFUPM), Kingdom of Saudi Arabia, in the Center for Refining & Advanced Chemicals of the Research Institute. He received his Ph.D. degree from Universiti Teknologi Malaysia in 2020. His current research focuses on the design of heterogeneous catalytic materials for applications such as the oxidation of methane, the conversion of CO<sub>2</sub>, the electrochemical reduction of CO<sub>2</sub>, the dry reforming of methane, and the splitting of water for hydrogen production.



Dr. Guowei ZHAO is currently serving as a full Professor in the College of Chemistry and Chemical Engineering, Huanggang Normal University, China. He received his Ph.D. degree in 2017 on all-solid-state batteries from Tokyo Institute of Technology, Japan, under the guidance of Prof. Kanno Ryoji. And then, continued his study on all-solid-state batteries as a Postdoc and research staff in Kanno's group until he moved back to China in March 2021. He is now interested in developing lithium conductive sulfides, oxides, and battery manufacturing technologies for all-solid-state batteries.

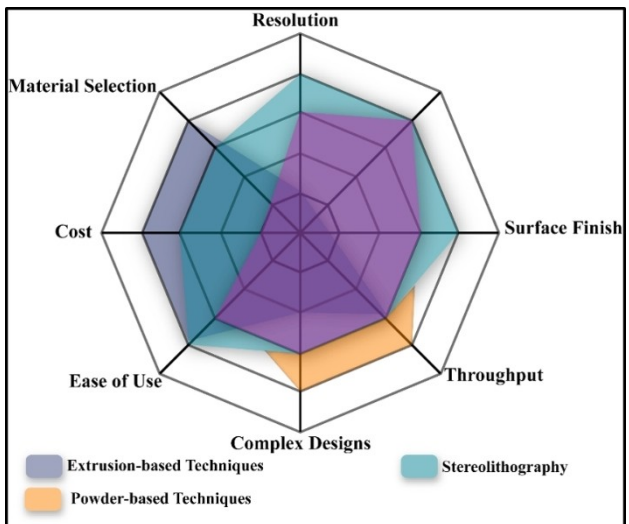


**Figure 1.** A spider web plot illustrating the essential factors to consider when selecting different 3D printing procedures. Reproduced with permission from Ref. [5]. Copyright (2021) Wiley-VCH.

to fabricating electrodes and other components in electrochemical energy storage.<sup>[20]</sup> A wide variety of 3D printing technologies, including robocasting or direct ink writing (DIW), select laser melting (SLM), inkjet printing (IJP), fused deposition modeling (FDM), and stereolithography (digital light processing (DLP) or stereolithography (SLA)), are developed and provided a high level of versatility for device fabrication in the field of energy storage.<sup>[21]</sup>

MEESDs, which include micro-supercapacitors (MSCs), micro-batteries (MBs), and metal-ion hybrid micro-supercapacitors (MIHMSCs), are key components of electronic systems. Herein, we focused on the latest advancements in 3D printing for MEESDs, such as MSCs, MBs, and MIHMSCs (Figure 2). Initially, this review discusses the fundamental of micro/nano energy storage devices by 3D printing technology. Then, emphasizes specific 3D printing techniques and their significance in advancements of MEESDs such as MSCs, MBs, and MIHMSCs with some advantages/disadvantages of each 3D printing technique. In the end, we present a conclusion along with some challenges and future prospects of 3D printing-based MEESDs, including material limitations, printing resolution, manufacturing scalability, mechanical properties and cost.

## 2. Fundamental of Micro/Nano Energy Storage Device by Additive Manufacturing (3D Printing)

MEESDs like MBs and MSCs typically comprise electrolyte, anode, cathode, current collector, and packaging components. 3D printing offers several unique benefits compared with more traditional methods of preparation to design a wide range of components of MEESDs, particularly the ability to fabricate fully

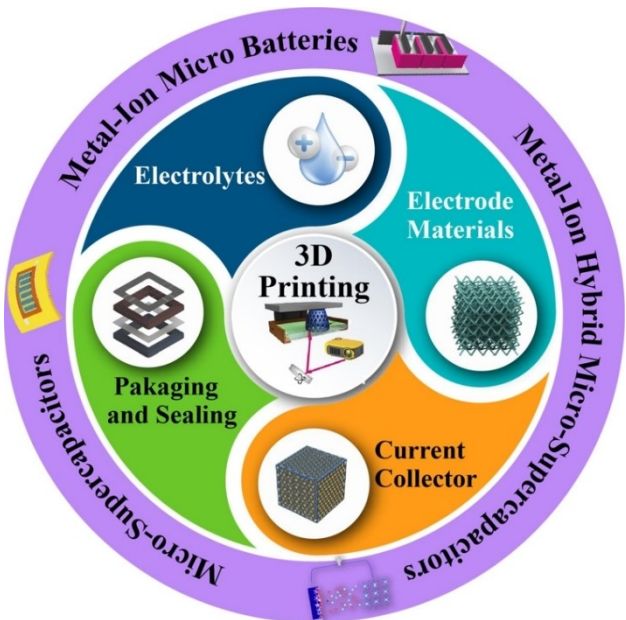


**Figure 2.** Schematic illustration of 3D printing technologies and their potential application in micro-electrochemical energy storage devices.

printed devices. The viscosity of printing ink must be adjusted to allow it to be seen as suitable, which can be possible by changing the amount and arrangement of the constituents. In the meantime, selecting an appropriate ink solvent is also crucial. The use of a variety of solvents will directly impact the dispersion of ink components. The use of stable inks that have a high storage modulus allows for structural integrity and continuous extrusion to be achieved during the printing process.

### 2.1. Electrode materials by 3D printing technology

The use of conventional electrode active materials, conductive additives and binders is required for their operation. Traditional preparation methods, including coating and calendaring, are employed to fabricate the planar electrode. Manufacturing various electrode materials is now more adaptable due to the versatility of 3D printing technology. Various materials can be treated using 3D printing technology, from inorganic, carbon and polymer to UV-curable resins. Some oxides, a class of inorganic semiconductors, can realize interesting new electrochemical reactivities. Polymers used for insulation could be served as supports or mould.<sup>[22]</sup> The electrode inks are more involved than the simple electrode slurry used previously. LiCo<sub>2</sub> (LCO),<sup>[23]</sup> LiTi<sub>5</sub>O<sub>12</sub> (LTO),<sup>[24]</sup> LiFePO<sub>4</sub> (LFP),<sup>[25]</sup> and polyaniline (PANI),<sup>[26]</sup> etc., are some of the most common active materials used for 3D printed electrodes. Electrode inks are essential for 3D printing electrodes of MEESDs. Cai et al.<sup>[27]</sup> developed sulfur/carbon/LaB<sub>6</sub> cathodes with a sulfur loading of 9.3 mg/cm<sup>2</sup> for Li–S batteries exhibiting a high areal capacity of 7.98 mAh/cm<sup>2</sup>. The rheological characteristics of inks are

often tuned through the application of graphene oxide (GO),<sup>[28]</sup> polymers,<sup>[29]</sup> cellulose,<sup>[30]</sup> and nanoparticles.<sup>[31]</sup> The active ingredients and compounds derived from GO have widespread usage in printing inks. Ink rheological characteristics are enhanced by using GO because of its high concentration of functional groups. The inks can benefit from the GO's many reaction sites, making them a suitable material for developing efficient hybrid inks. Composite inks for the interdigital MSC were designed by Liu et al.<sup>[32]</sup> via *in-situ* growth of vertically aligned PANI on the surface of GO. The manufactured MSC displayed high areal capacitance ( $153.6 \text{ mF/cm}^2$ ) and excellent capacitance retention (100% after 5000 cycles). Further details of electrode materials by 3D printing technology for MEESDs will be discussed in Section 3.

## 2.2. Electrolytes by 3D printing technology

Because interdigital electrodes have their unique structure, there is no need for a separator to be placed between either of these electrodes. To produce flexible planar MSCs, Bhattacharya et al.<sup>[33]</sup> proposed a manufacturing technique in which the electrodes (AC-Bi<sub>2</sub>O<sub>3</sub> and AC-MnO<sub>2</sub>), electrolyte (KOH/PVA), and reduced graphene oxide (rGO) layer were 3D printed using continuous inkjet printing (Figure 3a–c). The obtained MSCs showed an areal capacitance of  $536.6 \text{ mF/cm}^2$ , and a high specific energy density of  $15 \text{ mWh/cm}^3$  at a specific power density of  $0.14 \text{ W/cm}^3$ . Due to water electrolysis, the water-based electrolytes exhibited a tiny voltage window. Higher energy density in MSC devices is possible, thanks to the ionic-liquid-based gel electrolyte's higher ionic conductivity and operating voltage (up to 4 V). Their high-temperature tolerance also helps them to maintain their stability and safety in a variety of environments. Printing with such accuracy boosts the energy density of MEESDs and decreases material loss. Currently, 3D printing makes use of polymer,<sup>[34]</sup> ionic liquids,<sup>[35]</sup> and solid electrolytes.<sup>[36]</sup> In 3D-printed MSCs and MBs, gel polymers are frequently employed as electrolytes. Solvent evaporation, photopolymerization, and heat polymerization are all viable options for solidifying it on electrodes. The electrolytes can be assembled into devices by pouring, infiltrating and injecting.

Ionic liquid-based electrolytes were also employed in 3D printing to explore more about high-performance devices manufactured in their entirety. In addition, solid electrolytes are a kind of effective substitute for liquid electrolytes owing to their excellent safety and mechanical stability. However, these materials exhibit low ionic conductivity and high contact resistance, limiting their practical use.<sup>[39]</sup> This issue can be significantly reduced in severity by using 3D-printed solid-state electrolytes of various architectures. By the DIW method, McOwen et al.<sup>[38]</sup> manufactured Li<sub>7</sub>La<sub>3</sub>Zr<sub>2</sub>O<sub>12</sub> (LLZO) solid electrolytes with a wide range of microstructures. The printed electrolyte's arrangement and microstructure profoundly impact the ink's rheological characteristics. This ink was made by combining nanoscale LLZO particles with two distinct binder systems.

The first was a hexagonal-based composition, while the second was a polyvinyl butyral (PVB) binder with a benzyl butyl phthalate (BBP) plasticizer. The former binder approach resulted in inks with a conformal character, whereas the latter showed remarkable self-supporting capabilities. Lines, grids, and columns were printed from solid electrolytes using these two inks (Figure 3d–g). In addition, the symmetrical cell demonstrated a low and consistent overpotential at various current densities.

## 2.3. Current collectors by 3D printing technology

The active material is assembled with the current collector, which also collects the current it generates to create a larger external output. The active material should thus be entirely in contact with the current collector. Due to structural restrictions, conventional planar current collectors, for example metal foil, cannot offer an electrode material with a broader contact surface. A highly controlled microstructure could be printed on the collector using 3D printing technology, increasing the contact area. Rather than using a flat metal collector, energy storage devices could use direct printing with materials that improve performance. Using flashlight stringing technology, Chae et al.<sup>[40]</sup> produced an interdigital collector made of nickel nanoparticles. By creating an interdigital collector made of nickel nanoparticles, they were able to achieve an impressive areal specific energy of  $12.8 \text{ mWh/cm}^2$  at voltages up to 3 V. Additionally, it is suggested that the use of highly conductive metal particles for direct printing of electrodes could eliminate the need for a separate current collector.<sup>[41]</sup> The devices could be smaller by removing the inert component, and the increased percentage of active materials results in better specific energy.

## 2.4. "Packaging and Sealing" by 3D printing technology

The 3D printing of electrodes and electrolytes is currently receiving significant attention. However, it is also essential for energy storage devices to have proper packing materials that were manufactured with 3D printing technology. It can be packaged in the shape of a button or a soft pack, depending on the shape of the printed electrodes. Packaging materials, including polydimethylsiloxane (PDMS), polyethylene terephthalate (PET), and other polymers, are frequently employed to protect interdigital devices.<sup>[42]</sup> The repeatability of devices is decreased due to this technology, which includes imprecise operations such as transferring, aligning, and using a package of printed patterns. It is necessary to have proper packaging solutions for various shapes and sizes to design more precise energy storage devices. Materials employed for the packaging are significantly distinct from those used in producing functional components like electrodes and electrolytes. Through DIW technology, Chen et al.<sup>[43]</sup> printed a completely packaged SC on a flexible polyimide substrate. A carbon nanotube (CNT)

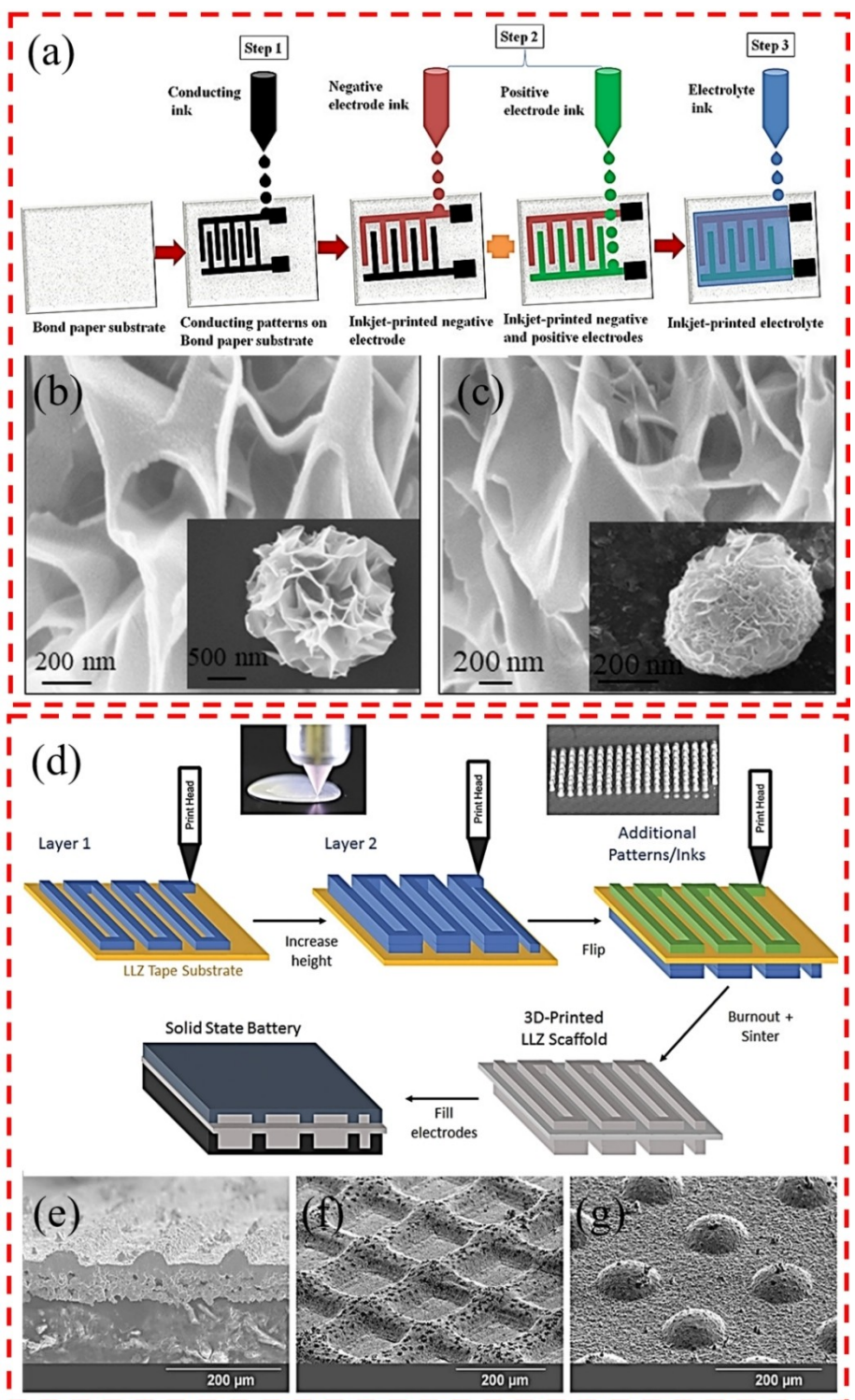


**Figure 3.** a) Step-by-step synthesis of an all-printed MSC on bond paper using multiple electrode and electrolyte materials, high-magnification scanning electron microscopy images of b)  $\text{Bi}_2\text{O}_3$ , and c) AC- $\text{Bi}_2\text{O}_3$ . Reproduced with permission from Ref. [37]. Copyright (2019) American Chemical Society. d) Schematic diagram of 3D printing solid electrolyte structures, e–g) SEM images of conformal ink-printed structures. Reproduced with permission from Ref. [38]. Copyright (2018) Wiley-VCH.

based electrode, PVA-based gel electrolyte, and silicone-gel packaging were sequentially manufactured on a flexible polyimide substrate using IJP technology. After being subjected to 1000 cycles, the packaged SC maintained

97.7% of its original capacitance, suggesting that the electrochemical performance was adversely affected.

### 3. Micro-Electrochemical Energy Storage Devices by 3D Printing

The recent exceptional breakthrough in 3D printed MEEDs demonstrates the promising future of 3D printing technology in manufacturing MEEDs. This is because 3D printing offers great promise for streamlining the manufacturing process and enabling more accurate, customized manufacture of MEEDs for higher electrochemical performance. In addition, 3D printing technologies are free of constraints by many limitations of traditional production processes, allowing for a much wider variety of geometrically demanding shape or configuration design options to be explored. This part focused on current developments in 3D-printed MEEDs such as MSCs, MBs, and MIHMCs. Additionally, the advantages and disadvantages of each specific 3D printing technique for MEEDs are critically analyzed.

#### 3.1. Micro-supercapacitors

The arrangement and composition of 3D-printed MSCs have influences on their electrochemical capabilities and possible applications. The two types of MSCs (namely, pseudocapacitors-based MSCs and electrochemical double layered-based MSCs) offer their benefits for micro-scale and nano-scale energy storage applications.

##### 3.1.1. Pseudocapacitance-based micro-supercapacitors

Pseudocapacitors are a promising type of energy storage device because they strike a good compromise between the two competing needs of high specific energy and rapid charge and discharge.<sup>[44]</sup> Pseudocapacitors are a special class of energy storage devices that utilize faradaic reactions at/or in close proximity to the electrode's surface to store energy. Commonly utilized materials for the pseudocapacitive electrodes include electrically conductive polymers, metals, and their oxides. Nevertheless, they typically work with a wide range of carbon-based compounds to enhance their electrical conductivity. Hybrid electrodes are often made by either composite printing ink from pre-mixed precursors or loading additional components onto printed scaffolds. Several other innovative two-dimensional (2D) nanomaterials other than graphene were investigated. These 2D materials include MXene and black phosphorus, etc. The following briefly overviews recent research on 3D printed MSCs employing pseudocapacitive active materials.

Manganese oxide ( $\text{MnO}_2$ ) is an excellent pseudocapacitive material owing to its exceptional theoretical specific capacitance, widespread availability, and little environmental impact.<sup>[45]</sup> Crystallinity engineering, morphological management, elemental doping, and defect introduction are some strategies employed to enhance  $\text{MnO}_2$ 's capacitive performance since its initial investigation by Lee and Goodenough in

1999.<sup>[46]</sup> The acquired specific capacitance was remarkable (between 150 and 600 F/g). However, capacitive performance often degrades drastically with increasing  $\text{MnO}_2$  loading because of difficulties with electron transport and ion diffusion.<sup>[47]</sup> The development of 3D printing processes opens new pathways for addressing this persistent issue with pseudocapacitors. Yao et al.<sup>[48]</sup> reported that pseudocapacitive  $\text{MnO}_2$  was supported by 3D-printed graphene aerogels, rationally prepared as a scaffold. Figure 4(a) shows the 3D printing process for graphene/ $\text{MnO}_2$  electrodes.

The DIW approach was used to print 3D GO structures using "ink", a mixture of GO solution (40 mg/mL) and 5% hydroxypropyl methylcellulose. The 3D-printed structures were subsequently treated through freeze-drying to yield aerogels. A thermal treatment process followed this in an atmosphere of nitrogen gas, which converted GO to graphene. The field emission scanning electron microscope (FESEM) image (Figure 4b and c) demonstrates that  $\text{MnO}_2$  is applied as a coating to the porous cylindrical rods. It is important to remember that  $\text{MnO}_2$  is deposited not only on the exterior of the lattice but also on its interior. Graphene aerogel, as evidenced by the uniform deposition of  $\text{MnO}_2$ , has high electrical conductivity and the 3D-printed lattice facilitates the rapid diffusion of electrolyte solution.

On the other hand, due to mass transport limitations in ion diffusion, most of the  $\text{MnO}_2$  is only deposited on the bulk graphene aerogel's external surface. The symmetric MSC devices were fabricated using two 3D G/ $\text{MnO}_2$  electrodes with a thickness of 4 mm. The device's galvanostatic charge/discharge (GCD) curves are triangular, indicating its pseudocapacitive signature activity (Figure 4d). Further, it provided a remarkable areal capacitance of 18.74 F/cm<sup>2</sup> at 1 mA/cm<sup>2</sup> and retained 67% of the initial value at 20 mA/cm<sup>2</sup>. In addition, any device needs to have a high level of cycle stability. After 20,000 cycles, the original capacitance of this symmetric device was preserved at a remarkable level of 92.9% (Figure 4e). The designed porous structure for effective ion transport and, as a result, permits ultrahigh mass loading of pseudocapacitive materials without compromising their capacitive performance. It highlights their significant practical application potential and potentially reinvents the standard layer-by-layer stacking production approach for commercial SCs.

Shen et al.<sup>[49]</sup> reported that an asymmetric MSC could be efficiently and accurately constructed by the 3D printing process. 3D printing processes of the asymmetric MSC with interdigital electrodes are depicted in Figure 4(f). First, active the cathode of material vanadium pentoxide ( $\text{V}_2\text{O}_5$ ) and the active anode of graphene-vanadium nitride quantum dots (G-VNQDs) were produced. The strong Faradaic activity and natural abundance of  $\text{V}_2\text{O}_5$  enable it to be used as a cathode. In contrast, the large pseudocapacitance and proper negative operating potential of VN enable it to be used as an anode. Subsequently, cathode or anode ink was produced by homogeneously blending  $\text{V}_2\text{O}_5$  or G-VNQDs with highly concentrated GO dispersions (50 mg/mL). This results in inks with high viscosity and shear-thinning rheological characteristics, which are suitable for extrusion-type 3D printing. The inks for two

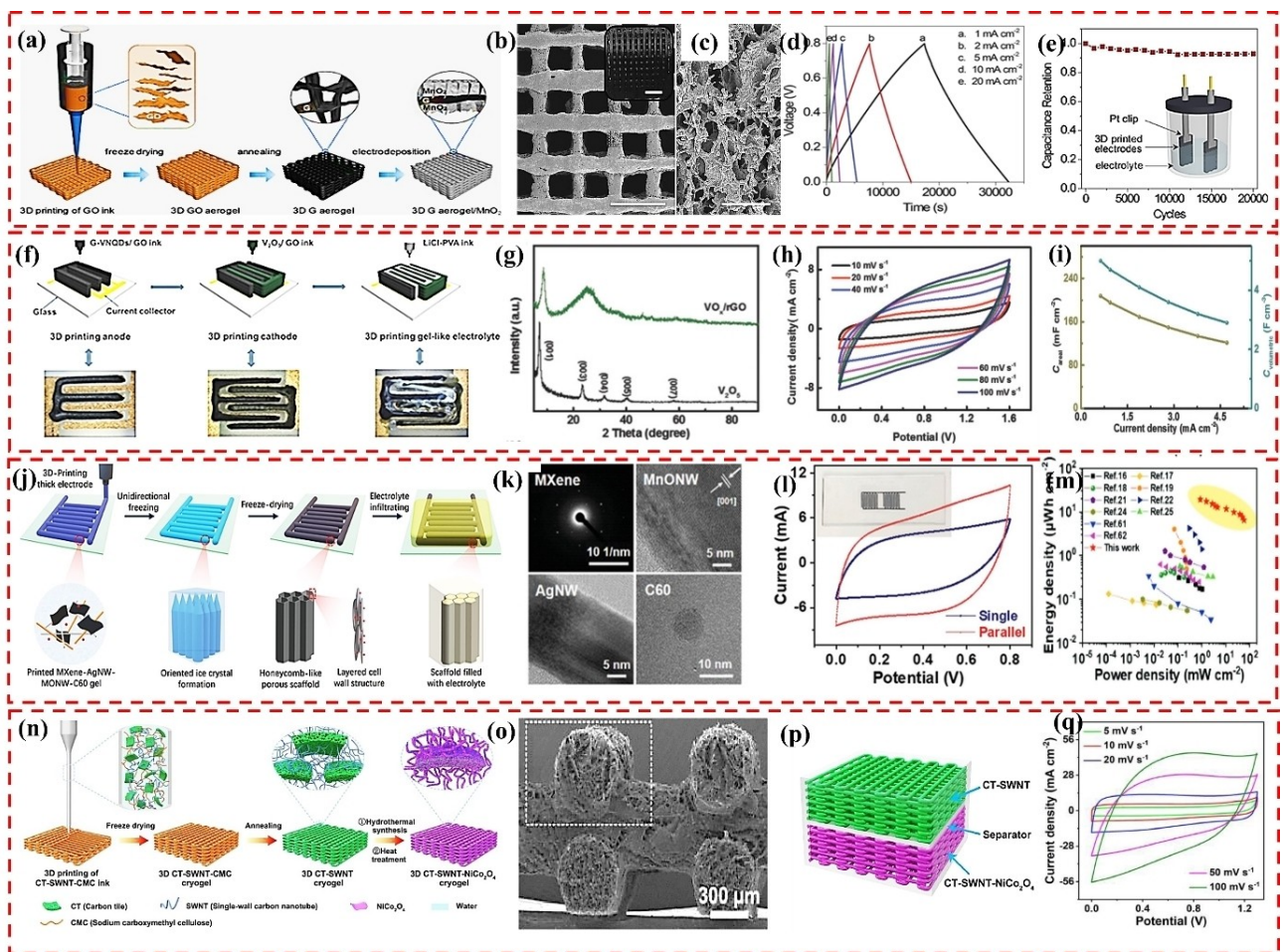


**Figure 4.** a) An illustration of the synthesis of a 3D printed graphene aerogel/MnO<sub>2</sub>, FESEM images at b) low-resolution and c) high-resolution. d) GCD of a symmetric device based on graphene aerogel/MnO<sub>2</sub>, e) Cycling stability test of aerogel/MnO<sub>2</sub> of a 2-mm-thick device tested at a scan rate of 20 mV/s for 20,000 cycles. Inset: schematic illustration of a symmetric supercapacitor device tested in aqueous electrolyte. Reproduced with permission from Ref. [48]. Copyright (2019) Elsevier. f) An interdigital electrostatic potential diagram of an asymmetric MSC printed via 3D printing, g) XRD patterns of pristine V<sub>2</sub>O<sub>5</sub> and VO<sub>x</sub>/rGO; h) CV curves of 3D printed VO<sub>x</sub>/rGO/G-VNQDs/rGO asymmetric MSC, i) The asymmetric MSC achieves a maximum full device areal and volumetric capacitance of 207.9 mF cm<sup>-2</sup> and 5.0 F cm<sup>-3</sup>, respectively. Reproduced with permission from Ref. [49]. Copyright (2019) Wiley-VCH. j) Schematic diagram of the synthesis of intrinsically stretchy MSCs via 3D printing and unidirectional freezing, k) SAED pattern and HRTEM images of the Ti<sub>3</sub>C<sub>2</sub>T<sub>x</sub>-MXene, AgNWs, MnO<sub>2</sub> NWs, and C<sub>60</sub> components, l) normalized CV curves obtained by measuring at 100 mV/s, m) Ragone plot. Reproduced with permission from Ref. [51]. Copyright (2020) Wiley-VCH. n) Schematic diagram of the synthesis of a 3D printed CT-SWNT-NiCo<sub>2</sub>O<sub>4</sub> cryogel electrode, o) SEM image, p) schematic diagram of assembled device, q) CV curves at different scan rates. Reproduced with permission from Ref. [52]. Copyright (2022) Elsevier.

electrodes were then placed in separated syringes with a capacity of 3 mL each, and they were extruded using air pressure via a nozzle with a diameter of 200  $\mu$ m so that they could be printed consecutively, layer-by-layer on the finger array current collectors. Afterward, a hydrazine hydrate gas reduction procedure was applied to produce rGO, and vacuum freeze-drying was used to remove the solvent from the 3D-printed structures so that they could be solidified.

Given that the V<sub>2</sub>O<sub>5</sub> might be decreased by the hydrazine hydrate simultaneously, the cathode and anode of the 3D printed battery were designated as VO<sub>x</sub>/rGO and G-VNQDs/rGO, respectively. Finally, the electrolyte, which had a gel consistency, was printed into the channels. This electrolyte also acted as a separator for the asymmetric MSC. Furthermore, in comparison with X-ray diffraction (XRD) patterns of pristine V<sub>2</sub>O<sub>5</sub>, VO<sub>x</sub>/rGO exhibits extra peaks at  $2\theta = 25.5^\circ$  and  $2\theta = 36.6^\circ$ ,  $47.1^\circ$ , and  $49.5^\circ$ , which were attributed to the presence of rGO

and V<sub>3</sub>O<sub>7</sub>, respectively (Figure 4g). The asymmetric MSC was constructed by performing a 3D printing process on a substrate using VO<sub>x</sub>/rGO as a cathode and G-VNQDs/rGO as an anode. The interdigital electrodes are four-layers thick with a mass density of 3.1 mg/cm<sup>2</sup>, contributing to their high mass density. The 3D-printed asymmetric MSC shows pseudo rectangular cyclic voltammogram (CV) curves without apparent redox peaks due to the strong capacitive characteristics of the VO<sub>x</sub>/rGO and G-VNQDs/rGO electrodes (Figure 4h). The device exhibits maximum areal and volumetric capacitances for the asymmetric MSC are 207.9 mF/cm<sup>2</sup> and 5.0 F/cm<sup>3</sup>, respectively. The printed asymmetric MSC's areal capacitance is around 10 times greater than that of a laser-writing asymmetric MSC.<sup>[50]</sup> The asymmetric MSCs exhibit an excellent rate performance with capacitance retention of 58.3% when the current density was increased from 0.63 to 4.71 mA/cm<sup>2</sup> (Figure 4i). Most significantly, an aerial-specific energy of 73.9  $\mu$ Wh/kg was

achieved. This straightforward, effective, and affordable method of designing asymmetric MSCs will meet the demand for high aerial-specific energy of next-generation micro-scale power units and significantly encourage their integration with on-chip energy storage systems. This 3D printing approach can be used to design several asymmetric MSCs to facilitate integration into on-chip energy storage systems.

The Liang group<sup>[51]</sup> demonstrated the fabrication of an intrinsically stretchable MSC through the 3D printing of a nanocomposite gel composed of  $Ti_3C_2T_x$ -MXene nanosheets, Ag nanowires (NWs),  $MnO_2$ NWs and fullerene. The gel was frozen in a unidirectional fashion to construct MSCs with thick and honeycomb-like porous interdigital electrodes ( $C_{60}$ ). Figure 4(j) shows advanced nanocomposite gelation techniques employed to create a viscous pseudoplastic MXene-based electrode ink for extrusion-based 3D printing. The process began with the selective etching of bulk  $Ti_3AlC_2$ -MAX, synthesizing hydrophilic and delaminated  $Ti_3C_2T_x$ -MXene nanosheets. To create the MXene-AgNW- $MnO_2$  NW- $C_{60}$  hydrogel, a moderately ultrasonicated mixture of MXene, Ag-NWs,  $MnO_2$ -NWs and  $C_{60}$  was synthesized, filtered through a vacuum, and then dispersed in deionized water. The rigid and hydrophobic 2D MXene nanosheets form a dynamic cross-linked 3D network with the pliable and hydrophilic one-dimensional (1D) Ag NWs and  $MnO_2$ -NWs. Ink made from printable nanocomposites does not require organic dispersants or rheological agents, thanks to this network's ability to promote gelation. Ag-NWs can be synthesized into a continuous conductive network to further speed up charge transport, while  $MnO_2$ -NWs provide high pseudocapacitance in nanocomposite electrodes. High-resolution transmission electron microscopy (HRTEM) images and selected area electron diffraction (SAED) patterns generated from the nanocomposite gel further verify all constituent elements' presence and even distribution (Figure 4(k)). Extremely transparent  $Ti_3C_2T_x$ -MXene nanosheets can be observed in the TEM image, and their hexagonal crystal symmetry is visible in the SAED pattern. An HRTEM image reveals that hydrothermally produced long  $MnO_2$ -NWs are monoclinic along the [001] direction. The TEM images also provide strong evidence for a uniformly distributed network of AgNWs and  $C_{60}$  nanoparticles, each of which has a layered structure and a diameter of roughly 7 nm.

These results demonstrated the development of a uniform ink formulation. By connecting multiple MSCs in series or in parallel, the output voltage and capacitance can be easily adjusted to meet the specific energy and power requirements of various energy storage devices. The high electrical conductivity of MXene-AgNWs- $MnO_2$ NWs- $C_{60}$  ink suggests its application use as a microelectrode I for MSCs, simplifying the system by eliminating the need for metal-based contacts or collectors. The potential benefits of interconnecting multiple MSCs were examined by connecting two MSCs in series and parallel. When connected in parallel, as shown in Figure 4(l), the CV curve remains within the same working voltage window, effectively doubling the capacitance. It has been confirmed that MXene-AgNWs- $MnO_2$ NWs- $C_{60}$  MSCs can be scaled up, and 3D printed MSCs have the potential to be integrated into

practical electronic devices due to the ease of modulating their properties through the combination of different MSCs. The MXene-Ag-NW- $MnO_2$ -NW- $C_{60}$  MSC's areal-specific energy and power densities are shown in Figure 4(m). With a specific power of 0.86 mW/cm<sup>2</sup>, it displayed a high areal specific energy of 19.2 Wh/cm<sup>2</sup>. These intrinsically stretchy MXene-Ag-NW- $MnO_2$ -NW- $C_{60}$  MSC exhibited high performance and a scalable and predictable manufacturing technique, making this strategy an exciting first step toward the widespread use of stretchable energy storage devices.

Yang et al.<sup>[52]</sup> used a controllable and scalable 3D printing technique to demonstrate the production of a new pseudocapacitive carbon tile (CT)-SWNT- $NiCo_2O_4$  electrode. The fabrication process of the 3D CT-SWNT- $NiCo_2O_4$  cryogel electrode is depicted in Figure 4(n), where a micro lattice structure with multiple orthogonal layers of parallel cylindrical rods was created by loading a highly concentrated mixture of ink, containing 2D CTs, 1D SWNTs, and sodium carboxymethyl cellulose (CMC) dispersant into a movable syringe barrel and extruding it through a nozzle continuously and uniformly. The 3D printed freestanding structure was protected from shrinking and deforming due to capillary pressure through an efficient freeze-drying strategy for water removal resulting in a porous and stable 3D architecture. Carbonization of CMC in the final 3D CT-SWNT-CMC cryogel resulted in a highly merged integration structure. In this structure, the crosslinked SWNTs are employed as bridges between porous CTs, creating a continuous conductive network and hierarchical porous structure. Additionally, annealing the cryogel enhances this structure, making it suitable as a scaffold for pseudocapacitive  $NiCo_2O_4$ , while maintaining a porous configuration. This results in the development of a 3D CT-SWNT- $NiCo_2O_4$  cryogel electrode. These electrodes were made possible by coupling CTs with highly conductive SWNTs, which resulted in a hierarchical porous network framework loaded with abundant pseudocapacitive  $NiCo_2O_4$ . High-performance pseudocapacitors could potentially benefit greatly from the use of this electrode. An examination of the cross-sectional SEM image of a CT-SWNT- $NiCo_2O_4$  cryogel electrode revealed that the filaments at the junction were tightly joined, resulting in a unified and cohesive structure (Figure 4(o)). The strong weld observed in the cross-sectional SEM image of the CT-SWNT- $NiCo_2O_4$  cryogel electrode is indicative of the overall stability of the electrode. Furthermore, the formation of  $NiCo_2O_4$  was observed to occur not only on the exterior surface but also throughout the entire interior of the micro lattice. To evaluate the practicality of the electrode, an asymmetric supercapacitor was developed using a CT-SWNT- $NiCo_2O_4$  anode, a CT-SWNT cathode, a 3501-polymer separator, and a 6 M KOH electrolyte as depicted in (Figure 4(p)). The pseudo rectangular shapes of the CV profiles as displayed in Figure 4(q) indicate that the as-fabricated device possesses exceptional capacitive properties, with an areal capacitance of 588 mF/cm<sup>2</sup> at 1 mA/cm<sup>2</sup> and still maintaining a capacitance of 390 mF/cm<sup>2</sup> at 20 mA/cm<sup>2</sup>. Additionally, the device displayed excellent rate performance. As an added bonus, the device can produce a peak-specific energy of 138 Wh/cm<sup>2</sup>. Remarkably, after 50,000 cycles, 82% of the

device's original capacity remained, and its Coulombic efficiency was 97.50%. The high capacity of the electrodes was reliably maintained even at extremely large thicknesses, which bodes well for their potential future uses. In addition, there is a growing body of literature on improving MSC's performance from a different aspect.<sup>[53]</sup>

### 3.1.2. Electrochemical double layered-based micro-supercapacitors

Electrochemical double-layer capacitors (EDLCs), also known as supercapacitors or electrochemical capacitors, are energy storage devices that utilize the electric double-layer effect to store charge. They can achieve high power densities due to their quick charging mechanism, which does not involve chemical reactions. EDLCs are commonly comprised of carbon-based materials such as activated carbon (AC). This is due to their advantageous properties such as chemical stability, mechanical strength, and high specific surface area. Furthermore, these materials can be engineered to exhibit controlled pore sizes, a high density of active sites for redox reactions, and customizable nanostructures. These characteristics make carbon-based materials highly desirable as electrode materials in EDLC-based energy storage systems, due to their potential for high performance.<sup>[54]</sup>

Graphene-based materials are extensively used as 3D printing electrodes for electrochemical double-layer capacitors-based MSCs due to their impressive characteristics.<sup>[55]</sup> These include a large surface area, high mechanical strength, and good electrical and thermal conductivities. The most common method of synthesizing graphene is extracting GO from graphite. This process may readily create GO in bigger quantities than the alternative way for more active sites, such as graphite exfoliation.<sup>[56]</sup> Good printing ability, a novel viscoelastic feature, and amphiphaticity distinguish GO, a key byproduct of graphene.<sup>[57]</sup> When GO is reduced to rGO, resulting in a material that is both hydrophilic and electrically conductive. Chemical reduction and heat reduction are two common techniques. Sun et al.<sup>[58]</sup> fabricated graphene-based interdigital microelectrodes for flexible planar EDLC-MSC by extruding GO ink and reducing it to rGO using hydroiodic acid. Capacitance was measured at around 56.5 F/cm<sup>3</sup> at 3 A/cm<sup>3</sup>, specific energy at 7 mWh/cm<sup>3</sup>, and specific power at 30 mW/cm<sup>3</sup>. Mattevi's group<sup>[59]</sup> demonstrated 3D-printed MSC electrodes prepared from pristine graphene aqueous inks without needing high-temperature processing or functional additions. As illustrated in Figure 5(a), the pristine graphene ink was used in producing woodpile electrodes with numerous layers for MSCs using DIW. As seen by the cross-sectional SEM image, the woodpile structure maintains its original form even after the printing and evaporation of the solvent. It is composed of parallel cylindrical rods composed of an interconnected network of pristine graphene platelets (Figure 5b). To further examine the electrochemical performance of pristine graphene electrodes, a symmetric MSC with increasing layers was designed. To construct the symmetric MSC, identical pristine graphene

electrodes with the same working surface (1 cm<sup>2</sup>) were used for the positive and negative electrodes. The electrolyte was an aqueous solution of 1 M lithium hydroxide (LiOH) (Figure 5c). Figure 5(d) displays the CV curves with 6 layers of symmetric devices. The CV curves have a rectangular shape at low scan rates, with slight profile distortion at higher scan rates. The maximal cell voltage of the 3D printed MSC is 1.0 V, and their capacitance is 1.57 F/cm<sup>2</sup>. In addition, the stability testing and kinetic analyses proved the high performance of our pristine graphene-based devices. These tests indicated that the electrodes had a higher voltage holding capability and a rapid charge transit rate. The greatest areal specific energy and power of 51.2 µWh/cm<sup>2</sup> and 0.968 mW/cm<sup>2</sup>, respectively, were also demonstrated by the 3D-printed MSC.

Yuan et al. proposed that creating 3D-printed carbon aerogel (CA) micro lattices with variable thicknesses is an effective method for achieving high areal capacitance.<sup>[60]</sup> The authors also reported that using GO/polyamic acid (GP) ink, with polyamic acid (PAA) serving as a crosslinker, allowed for the production of self-supported and programmable 3D structures with optimal printability and formability. Figure 5(e) depicts a schematic representation of the 3D-printed CA preparation method. During the freeze-drying process, ice crystals on the surface of the CA material sublimated, resulting in the formation of homogeneous macropores (Figure 5f). This allows for better penetration of the electrolyte into the electrodes. Further, a fast electrochemical response was achieved using the macropores as ion storage buffers and the linked network to speedup ion transport. The designed symmetrical SCs were further evaluated using a two-electrode setup with a 6-layer CA micro lattice as the electrode to determine the real performance of the entire device as displayed in (Figure 5g). The symmetrical device based on the CA micro lattice exhibits dominating performance, as evidenced by its superior areal capacitance and areal specific energy compared with those of most previously described carbon-based devices, as illustrated in (Figure 5h).

Zhu et al.<sup>[61]</sup> presented a method for producing 3D-printed graphene composite aerogels (3D-GCAs) with a structure optimized for MSC. Using a radio-frequency-based (RF) catalyst, silica powder, and graphene nanoplatelets, 3D-GCAs created GO ink. To avoid the structural shrinkage that will occur if the ink hadn't been printed in an isoctane solution after being carbonized at a high temperature for reduction (Figure 5i). As shown in Figure 5(j), the aerogel containing 16.7 wt% graphene nanoparticles (GNP) exhibits a highly brittle nature, which should be attributed to the loss of the elastic properties of the graphene-like network. The CV curves, recorded over a range of scan rates from 10 to 500 mV/s, exhibit a nearly rectangular shape as shown in (Figure 5k). To construct a symmetric SC, two identical GO-GNP-SiO<sub>2</sub> electrodes were joined using a thin separator, as illustrated in the inset of (Figure 5l). These results demonstrate that the device exhibited exceptional specific power of 4079.9 W/kg, specific energy of 0.43 Wh/kg, and a specific field of 4.76 F/g at a current density of 0.4 A/g. Even when the current density was increased by a factor of 20 (8 A/

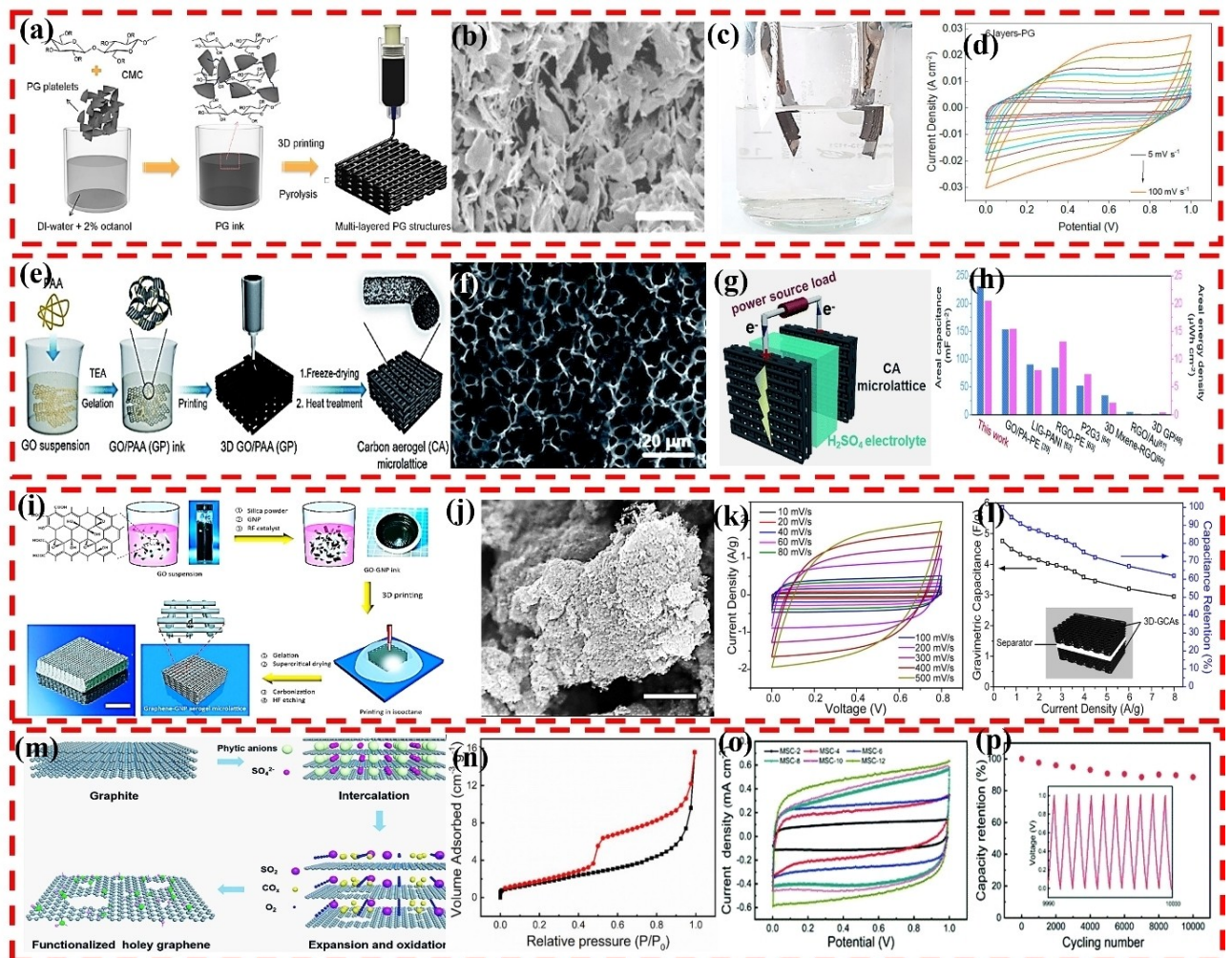


**Figure 5.** a) Schematic diagram and b) the SEM image of the formulation and 3D printing of the pristine graphene ink; c) Schematic of the symmetrical two-electrode testing method and d) CV curves for pristine graphene woodpile electrodes. Reproduced with permission from Ref. [59]. Copyright (2021) American Chemical Society. e) Schematic diagram for the synthesis of the CA micro lattice, and f) its SEM image, g) Schematic diagram of a symmetric MSC, h) comparison of the areal specific capacitance and areal specific energy. Reproduced with permission from Ref. [60]. Copyright (2021) Royal Society of Chemistry. i) Schematic diagram of the synthesis method of GNP aerogel micro-lattice, and j) the corresponding SEM image, k) CV curves of 3D-GCA, l) gravimetric capacitance vs. current density of symmetric SC in the inset. Reproduced with permission from Ref. [61]. Copyright (2016) American Chemical Society. m) Process of electrochemical exfoliation of synthesis of FHG, n)  $N_2$  sorption isotherm, o) CV curves of MSCs with different thicknesses at 100 mV/s, p) cycling stability. Reproduced with permission from Ref. [62]. Copyright (2019) Royal Society of Chemistry.

g), 61% of the maximum gravimetric capacitance of 2.95 F/g was still retained.

Yu et al.<sup>[62]</sup> described a hierarchical porous electrochemically exfoliated O, P-functionalized holey graphene (FHG) structure for high-performance flexible MSC electrodes. Figure 5(m) illustrates the preparation procedure for FHG, which includes the processes of exfoliation, functionalization, and hole formation. The nitrogen ( $N_2$ ) sorption isotherm indicates the mesopores and macropores, as shown in Figure 5(n). These perforations shorten the path ions which travel to diffuse through the material, improving electrochemical performance. To determine the impact of thickness on capacitance, a variety of in-plane interdigital MSCs were constructed with varying thicknesses. Figure 5(o) depicts the CV profiles of devices with a variety of thicknesses, at 100 mV/s. All of the CV curves have a nearly rectangular CV shape, signifying excellent electro-

chemical performance, and the enclosed area of the CV curves enlarges as the electrode thickness increases. The MSC demonstrated the maximum areal capacitance of 6.41 mF/cm<sup>2</sup> when measured at 0.05 mA/cm<sup>2</sup>. The MSC has remarkable cycling stability, retaining over 88.6% of its original capacitance after 10,000 cycles (Figure 5p). The normal cycle from 9990 to 10,000 are depicted in the inset, and no significant distortion is visible in comparison with the original. The remarkable performance of the MSCs illustrates the potential for graphene to be used in developing flexible, portable, and wearable electronic systems. The 3D-printed GO electrodes were used in similar investigations, which also reported MSCs with interdigitated or in-plane topologies.<sup>[63]</sup>

The 3D printing techniques including IJP, DIW, freeze drying, FDM, and MJ used to fabricate the electrode material for MSCs have their merits and demerits. The IJP technique

allows for rapid, fast prototyping, digital pattern customization, high throughput, high precision, scalable, flexibility, high uniformity and reproducibility, little material waste, non-contact, and mask-free. However, IJP requires expensive equipment, high requirements for ink, and nozzles prone to clogging are its main limitations for commercial applications. DIW provides an economical solution to the fabrication because of its easy operation, wide material diversity, and no mask requirement, but stringent requirements for ink are one of the main limitations. Freeze drying possesses some advantages of preservation of the structure, preservation of chemical properties, high porosity, and reduced shrinkage. However, slow process, limited scalability, limited material options, and high-cost fabrications are its main drawbacks. FDM provides accessibility, ease of use material flexibility and customizability are its merits. But, limited strength and durability, limited resolution, surface quality, limited size, and poor surface quality are its main drawbacks. MJ 3D offers many advantages such as smooth surface finish, high resolution and precision, high speed, materials flexibility, and customizability of fabrication of microelectrochemical devices but limited built volume, post-processing requirements, and material handling are major issues that lead to inconsistent electrochemical performance and lower cyclic stabilities.

### 3.2. Metal-ion micro-batteries

#### 3.2.1. Lithium-ion micro batteries

Lithium-ion batteries (LIBs) have attracted significant attention in recent decades due to their high specific energy, low weight, and prolonged cycle life at high current densities.<sup>[64]</sup> Furthermore, developing novel manufacturing techniques for micro-batteries (MBs) that possess arbitrary design, low cost, and improved electrochemical performance has gained significant attention in recent years.<sup>[65]</sup> Sun et al.<sup>[66]</sup> were the first to successfully fabricate an interdigital Li-ion micro-battery (LIMB) using a DIW in 2013. The micro-battery was constructed using lithium titanate (LTO) as the anode and lithium iron phosphate (LFP) as the cathode and exhibited a capacity of 1.2 mAh/cm<sup>2</sup> at 0.5 C, an areal specific energy of 9.7 J/cm<sup>2</sup>, and a specific power of 2.7 mW/cm<sup>2</sup>. Wu's research group<sup>[67]</sup> reported the scalable fabrication of multi-layer printable lithium-ion MB (LIMB) by highly conductive and mechanically stable inks. This was achieved by fully incorporating polyurethane binders with graphene and CNTs high-conducting additives into active materials to construct a cross-linked conductive network. Customized screen-printing inks, such as LFP@GC ink (Figure 6a), were created by homogeneously mixing active ingredients (LFP or LTO), conductive carbon, graphene, and CNTs with polyurethane and dibasic ester. According to cross-sectional SEM images, the one-layer printed microelectrodes of LFP@GC-LIMBs have a thickness of around 32 µm (Figure 6b). The LIMBs with volumetric specific energy will reach a maximum value of 108.2 mWh/cm<sup>3</sup> (Figure 6c), strikingly competitive with the previously stated typical values. A smart

bracelet made up of a serially-connected device, a temperature sensor, and an LED was able to determine a precise temperature because of its high degree of integration. The temperature sensor can detect the signal to bridge the integrated circuits and switch on the associated LED when the temperature is over 37°C (Figure 6d). These kinds of efforts will give a fresh perspective on using screen-printed inks that are highly conductive and mechanically stable to produce MBs with a high areal specific energy for wearable smart devices.

Highly capacitive electrodes, metal-free current collectors, sensitive sensing materials, conductive interconnectors, and adhesive additives are all demonstrated by Zheng et al.<sup>[68]</sup> using aqueous printable multifunctional MXene inks. High output and precise ink deposition are possible with a well-designed screen-printing process. To fabricate MXene-based LIMB, the aqueous MXene-based LTO and LFP inks were printed in a sequential manner on both sides of MXene-based current collectors as depicted in Figure 6(e). The diffraction peaks in XRD patterns of printed MXene-based LTO and LFP microelectrodes, as shown in Figure 6(f), indicate the presence of both MXene and LTO or LFP, indicating that there is close contact between the current collectors and the microelectrodes as depicted in Figure 6(g). Microelectrodes also showed that the LTO and LFP particles were uniformly distributed throughout the framework of the conducting MXene nanosheet. The printing process as a whole did not involve using any organic solvents, conductive additives, or binder polymers. This demonstrates the environmentally friendly nature of MB's production method. The highly malleable scaffold created by MXene enables MXene-based LIMB to exhibit exceptional flexibility without any loss of capacity even after being repeatedly bent for 1000 cycles as shown in Figure 6(h). MXene-LIMBs also demonstrate good cyclability, with a capacity retention of 82% after 1000 cycles as shown in Figure 6(i). Using printable multitasking MXene inks will open up new possibilities for the scalable fabrication of devices and systems that integrate various functions, with broad applications in optoelectronics, energy storage, sensing, and electronics.

Biro's group<sup>[69]</sup> recently demonstrated slurries with a high silicon/carbon-graphite (Si/C-graphite) combination used in 3D-printed LIMBs. Adjusting the thickness of the electrodes in traditional batteries with flat electrodes allows for the optimization of either the specific power output or the specific energy. Figure 6(j) provides a visual representation of the fundamental concept underlying 3D printed MBs. SEM image of printed 8-layer structures with 24 wt% binders is shown in Figure 6(k). The aspect ratio (appearing as "sharpness") of the structure improves as the binder content rises. Cycling tests were carried out using a standard coin cell set up to evaluate the electrochemical performance of Si/C-graphite blend anodes for use in 3D-printed LIMB. The capacity values, depicted in Figure 6(l), vary depending on the amount of binder used. After 65 cycles, the anode demonstrates stable cycling with a current density of 484 mAh/g and a capacity retention of 99.4%. Anodes with 6 wt% and 12 wt%, binder demonstrate good capacity retention of 90% and 89% at a current rate of 4C compared to cycling at C/4, indicating a reduced internal resistance

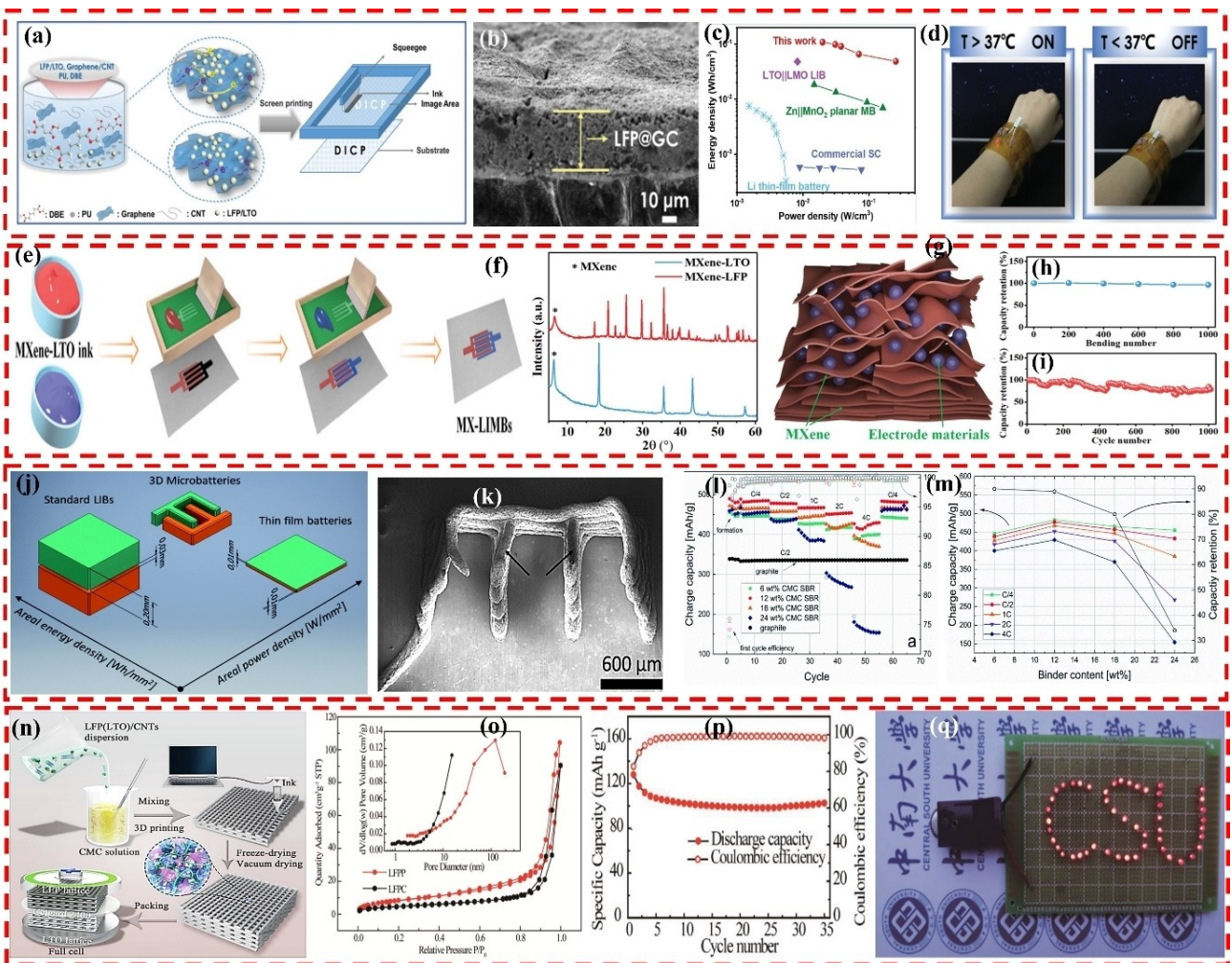


**Figure 6.** a) Schematic diagram of the components of LFP/LTO@GC and LFP/LTO@G inks, b) SEM image, c) specific energy vs. specific power, d) smart bracelet with rechargeable LIMB, temperature sensor, and LED. Reproduced with permission from Ref. [66]. Copyright (2021) Wiley. e) Schematic diagram and f) XRD patterns of the synthesis of MXene-LIMBs. g) Schematic diagram of the printed microelectrodes, h) capacity retention with repeated bending, and i) cycling stability. Reproduced with permission from Ref. [68]. Copyright (2021) Wiley. j) Fundamental concept behind battery optimization for 3D printing, the dimensions presented provide a scale for the electrode thickness, k) SEM image, l) rate performance, m) charge capacity, and capacity retention. Reproduced with permission from Ref. [69]. Copyright (2020) Royal Society of Chemistry. n) Schematic diagram of 3D printed microelectrodes and full LIMBs, o) N<sub>2</sub> sorption isotherm, p) cycling stability, q) lighted LEDs with a pattern of CSU. Reproduced with permission from Ref. [70]. Copyright (2018) Wiley.

compared with anodes with higher binder concentration. Figure 6(m) summarizes the cell results for ease of comparison. After 65 cycles of all samples, the overall capacity retention is close to 100%, which implies minimal permanent capacity losses with fast charging. At C/4, the sample with 6 wt% binders has the lowest capacity. However, the capacity loss at increased C-rates is similar to the sample with 12 wt% binders, indicating that low capacity does not necessarily equate to high internal resistance. A counteractive process occurred, resulting in low-capacity numbers. The electrochemical suitability of this system for Si-based anodes is enhanced by the dispenser printing process's ability to promote ad- and cohesive characteristics.

Chen's research group<sup>[70]</sup> reported that by utilizing 3D DIW and freeze-drying procedures, 3D architected microelectrodes can be fabricated and achieved high areal capacity for LIMBs. A schematic diagram of 3D printed micro-lattices for LIMBs is

depicted in Figure 6(n). The process involved mixing the CNTs dispersion, active powder (LFP or LTO), and carboxymethylcellulose sodium (CMC) solution using magnetic stirring to create homogeneous dispersions. To create 3D DIW inks with the necessary rheological properties, the dispersions were evaporated and kept in syringes to be used for printing micro-lattices. The lattices were immediately formed into cells after undergoing freeze-drying and vacuum-drying processes. Figure 6(o) shows that when compared with the pore distribution curve of LFPC, the curve of LFPP moves to the right, indicating that LFPP contains larger pores, while the LFPC has pores smaller than 15 nm. Surface tension caused by direct drying in an oven causes the interspace to contract, whereas freeze-drying does not. Therefore, the freeze-dried LFPP maintains larger and more numerous pores, which improves the electrolyte penetration and allows Li<sup>+</sup> to move and transport freely over the entire electrode. Additionally, the 3D-printed micro-

electrodes retain their higher areal loading of  $32 \text{ mg/cm}^2$  and high gravimetric capacity, achieving a high areal capacity of  $5.05 \text{ mAh/cm}^2$ . Figure 6(p) illustrates the cycle stability of the device, which shows an initial discharge capacity of  $128 \text{ mAh/g}$  and a coulombic efficiency of 82.7%. After several cycles, the coulombic efficiency eventually stabilizes at around 99%. Additionally, after 35 cycles, the device has maintained its initial capacity of  $102 \text{ mAh/g}$ . An assembled device was used to demonstrate the feasibility of 3D printed complete cells by lighting a series of LEDs in the pattern of "CSU" (Central South University) as shown in Figure 6(q). The ink preparation method and the accessible 3D printing technology can be further applied to a wider range of active materials, which offers significant potential for manufacturing more sophisticated 3D structures for advanced LIMBs.

### 3.2.2. Sodium-ion micro-batteries

The development of rechargeable sodium-ion micro-batteries (NIMBs) with cathode and anode placement on the same substrate in a planar format has the potential to power coplanar microelectronics. However, this is hindered by the low areal capacity caused by thin microelectrodes. The sodium resources are abundant, the cost is low, the solvation shell is small, and the underlying principle of NIMBs is similar to that of the market-leading LIMBs, making them a promising type of rechargeable MB. The microelectrodes that makeup NIMBs are placed in an interdigital space.<sup>[71]</sup> Interdigital NIMBs that are both flexible and electrically conductive can now be printed in 3D, as described by Ma et al.<sup>[72]</sup> Planar NIMBs, which include the cathode, anode, and electrolyte, can be fabricated using 3D printing, as depicted in Figure 7(a). This was achieved by obtaining high-conductive 2D exfoliated graphene (EG) and 1D

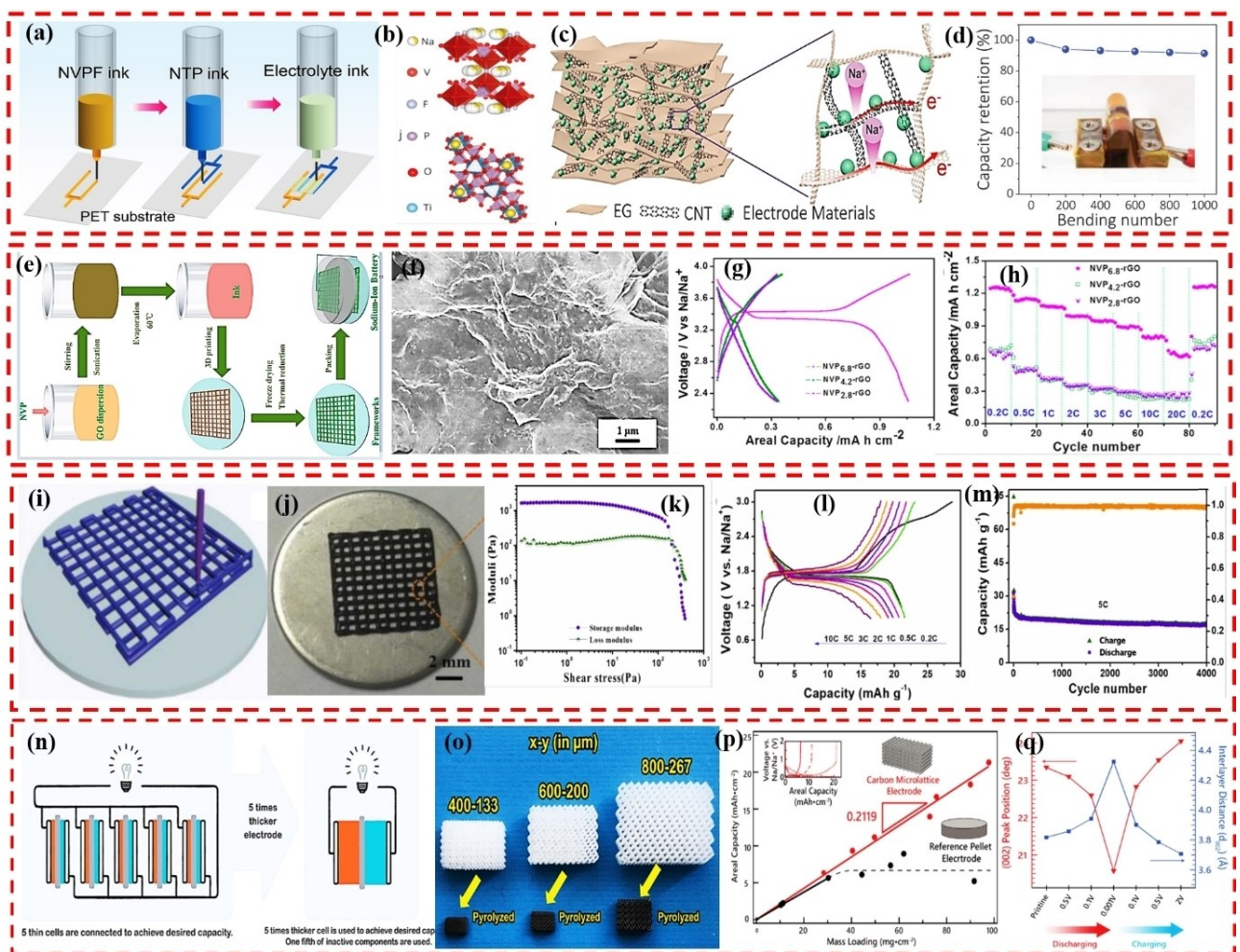


**Figure 7.** a) Schematic of 3D printing NVPF, NTP, and ionogel inks NIMB/EC || NVPF || IE, b) schematic diagram of the NVPF crystal structure, c) microelectrodes based on conductive EG nanosheets and CNT, d) retention of capacity as a function of the number of repeated bends. Reproduced with permission from Ref. [72]. Copyright (2022) Wiley. e) Schematic diagram of 3D printed porous hierarchies, f) high-magnification SEM images, g) selected 10<sup>th</sup> GCD curves at 2 C, h) rate performance of 3D-printed NVP-rGO frameworks. Reproduced with permission from Ref. [74]. Copyright (2017) American Chemical Society. 3D printed cubic-lattice filament networks: i) schematic and j) optical images, k) NVP ink curves, l) the relationship between voltage and capacity from 0.2 to 10 C, and m) cycling stability. Reproduced with permission from Ref. [75]. Copyright (2022) Elsevier. n) Schematic of thin and thick electrode cell assemblies, o) 3D printed resin and carbon micro lattice electrodes (below). The bottom scale is 1 mm. p) 400-133 carbon micro lattice electrodes and reference pellet electrodes mass loading against areal capacity plot, q) (002) peak position and interlayer distance ( $d_{002}$ ). Reproduced with permission from Ref. [77]. Copyright (2022) Wiley.

CNTs by dispersing  $\text{Na}_3\text{V}_2(\text{PO}_4)_2\text{O}_2\text{F}$  (NVPF) cuboids or  $\text{NaTi}_2(\text{PO}_4)_3$  (NTP) nanoparticles in deionized water, ethylene glycol, and CMC binder to create printable aqueous gel-like cathode and anode inks. These inks, referred to as NVPF/EC and NTP/EC, have desirable rheological properties and do not contain harmful solvents. They were used to print interdigital NIMBs with a custom microelectrode thickness, by utilizing electrochemically active particles combined with highly conductive 2D EG and 1D CNTs to form a 3D hierarchically conductive framework, which facilitates rapid electron transfer and ion diffusion. The high degree of adaptability of 3D-printed NIMBs is demonstrated by their ability to withstand bending and twisting without exfoliating from the substrate. This is attributed to the use of a Na-super-ionic conductor (NASICON) framework for rapid Na-ion transfer as depicted in Figure 7(b) and a stable structure with a high voltage plateau as reasons for choosing NVPF as the cathode.<sup>[73]</sup> Electrochemically, NVPF ||  $\text{NaBF}_4\text{-IE}$  || NTP NIMB/EC-2 L outperforms NVPF ||  $\text{NaBF}_4\text{-IE}$  || NTP NIMB/E-2 L due to its elaborate 3D conductive framework with 2D EG nanosheets and 1D CNTs, which forms an efficient conductive network with high electrical conductivity and low resistance as shown in Figure 7(c). The initial capacity is maintained at 91% even after being repeatedly bent over a thousand times (Figure 7d), indicating the material's high interfacial coupling and strong mechanical flexibility. This justifies the development of high-performance planar NIMBs via 3D printing methods for the next-generation wearable and portable microelectronics.

As described by Yang's group<sup>[74]</sup> using specially developed inks containing GO through 3D printing have been utilized to create novel hierarchical porous frameworks for salt storage. These frameworks are 3D printed as depicted in Figure 7(e). Specifically, homogeneous GO-containing inks with appropriate rheological properties were prepared by immobilizing GO at a concentration of 20 mg/mL and adjusting the concentrations of NVP (a material with a sodium storage capacity of 117.6 mAh/g) from 180, 47 to 20 mg/mL. The aforementioned GO-containing inks were then used with a 200  $\mu\text{m}$ -diameter nozzle attached to a 3D printing workstation to print layer-by-layer frameworks on stainless steel sheets. These frameworks were subsequently freeze-dried under controlled conditions and thermally treated to reduced GO, resulting in hierarchical porous frameworks. A high-magnification SEM image (Figure 7f) demonstrates the evenly distributed NVP particles throughout the frameworks. Galvanostatic charge-discharge (GCD) studies were conducted at scan rates ranging from 0.2 to 20 C, (1 C = 2.1 mAh/cm<sup>2</sup>) with a focus on the electrochemical performance of 3D printed NVP-rGO frameworks for  $\text{Na}^+$  storage. Specifically, the NVP6.8-rGO framework demonstrated a remarkably high capacity of 1.26 mAh/cm<sup>2</sup> at a rate of 0.2 C, which is higher than that of the NVP4.2-rGO and NVP2.8-rGO frameworks, which were approximately 0.67 mAh/cm<sup>2</sup> and 0.89 mAh/cm<sup>2</sup>, respectively as shown in Figure 7(g).

Additionally, even when the rate increased to 5 C, the NVP6.8-rGO framework still demonstrated a high capacity of 0.65 mAh/cm<sup>2</sup>. The electrochemical performance of a 3D-printed NVP-rGO framework for sodium storage was studied.

The hierarchical porous structure of the framework, created using a specially developed GO-containing ink and a 3D printing method, was found to effectively shorten the transportation of sodium ions, resulting in a high-rate capability. The framework demonstrated a capacity of 1.26 mAh/cm<sup>2</sup> at a low current rate of 0.2 C and maintained a capacity of 0.89 mAh/cm<sup>2</sup> at a high current rate of 5 C (Figure 7h). Additionally, the framework exhibited high reversible capacities and steady cycle performance as both the cathode and the anode, suggesting great potential in a broad range of applications.

According to the research Ding group<sup>[75]</sup> sodium-ion microbatteries (SIMBs) can be easily fabricated using 3D printing and polymer-based inks with a high amount of active material. The cubic-lattice filaments were initially 3D printed using a technique to create full-cell SIMBs (Figure 7i and j). The cubic-lattice filaments had a diameter ( $d$ ) of  $\sim$ 0.2 mm and the distance ( $L$ ) between adjacent filaments was  $\sim$ 0.8 mm. The resulting filaments exhibited consistent dispersion of active material. Importantly, the NVP ink had a shear-thinning feature, indicating that it was composed of non-Newtonian fluids and was suitable for 3D printing as depicted in Figure 7(k).<sup>[76]</sup> To demonstrate the viability of the 3D-printed NVP cathode and anode, full SIMBs were designed and tested. The capacities were 19, 18, 17, and 15 mAh/g when the current densities increased from 1, 2, 3, and 10 C, respectively (Figure 7l). The full SIMBs had a capacity retention rate of 55% (from 31 to 17 mAh/g) and could operate for 4000 cycles at 5 C (Figure 7m). Compared with conventional coating-based batteries, the electrochemical performance of full-cell SIMBs was satisfactory, taking the high loading of active material per unit area based on the total mass of the cathode and anode into account. This approach can create a wide variety of batteries, including ultra-micro, large-size, and even unconventional varieties.

The Kaner group<sup>[77]</sup> utilized a low-cost 3D printer to fabricate nitrogen-doped mesoporous biochar constructed from rigid carbon micro lattices. These microchannels enhance ion transport and permit the controlled fabrication of periodic carbon micro lattices. One strategy for achieving improved performance is increasing the bulk loading of active elements within a single cell. This strategy was realized by utilizing the standard film electrode production technique, which employs a slurry consisting of active elements in powder form. However, this approach is limited by the maximal functional thickness of the electrode, as the rates of ion transport are constrained and the performance of the battery will suffer from increased resistance and overpotential.<sup>[78]</sup> Additionally, the slurry's constituent parts may begin to settle, leading to the migration and localization of the binder at the electrode surface after drying, which results in degraded battery performance and, in extreme cases, electrical connections becoming severed, resulting in battery failure.<sup>[79]</sup> In this investigation, samples were labeled as "x-y" to denote the lengths of the unit cells and beam widths of each 3D model, specifically 400–133, 600–200, and 800–267, as depicted in Figure 7(n). The white micro-lattices on the pedestal are resin samples that have been removed and replicate the architectural characteristics of the initial 3D model. Despite experiencing linear shrinkage of approximately 70%

75% in each direction, the micro-lattices retained their integral structure throughout the pyrolysis process (Figure 7o). The 400–133 electrodes exhibited a well-defined plateau region and achieved normal gravimetric capacities for  $\text{Na}^+$  storage at all investigated mass loadings, reaching capacities of around 200 mAh/g. The areal capacity increased linearly following the mass loading, reaching a record-high value of 21.3 mAh/cm<sup>2</sup> at a mass loading of mAh/cm<sup>2</sup> (Figure 7p and the inset). The correlation coefficient of  $R_2=0.97$  in Figure 7(p)'s red trend line with the intercept at the origin indicates an ideal linear relationship between the areal capacity and the mass loading, demonstrating that the 3D microarchitecture facilitated efficient  $\text{Na}^+$  transport and utilization of the entire mass regardless of the nominal thickness of the micro-lattices. Figure 7(q) summarizes the variations in the placements of (002) peak and corresponding interlayer distances. As a result of the reaction in the plateau region, the interlayer distance of the carbon sheets increased, indicating intercalation. Throughout the process, there was no discernible shift in the position of the (100) peak. The interlayer distance at 2 V after charging was found to be 0.1 Å, smaller than that at the initial pristine state. This structural change should be attributed to the relaxation of residual tension that accumulates inside pyrolytic carbon obtained from photoresist resins, which can arise from the reaction between pyrolytic carbon and photoresist resins. From a practical and theoretical standpoint, carbon micro lattice electrodes may offer a viable solution for advancing green energy.

### 3.2.3. Zinc-ion microbatteries

In addition to LIMBs and NIMBs, there is considerable research on various multivalent cation metal batteries, such as zinc-based, magnesium-based, and aluminum-based batteries, in recent years. These small batteries possess high specific energy, are noncombustible, resistant to moisture, have abundant ground storage, and are relatively inexpensive.<sup>[80]</sup> However, there has been limited research on the 3D printing of zinc-based electrodes, such as Zn–Ag, Zn-metal oxide, and Zn-air systems, as the 3D printing of multivalent cation MBs is still in its early stages of development.<sup>[81]</sup> Weng et al.<sup>[82]</sup> disclosed a straightforward and effective method to create flexible Zn-ion microbatteries (ZIMBs) based on customized soft templates. These templates are designed by engraving, which enables the ZIMBs to be designed with various shapes and on a variety of substrates. Figure 8(a) depicts the fabrication procedure of ZIMB. A piece of adhesive paper was inserted into an engraving tool and a design was cut into it. The substrates were first printed, and then a conductive layer was placed in the pattern-restriction areas using a silver slurry. After that, the silver collectors were coated consistently with MnS and Zn powders. The patterned electrodes were extracted from the self-adhesive soft template, which was then revealed. It was pointed out that maintaining the electrodes' stable electrochemical performances requires a full dry stage. Following the application of the gel electrolyte electrodes, completed ZIMBs were manufac-

tured. Figure 8(b) demonstrates the ZIMB's operating concept while depicting a typical interdigital ZIMB, a hydrothermal synthesis approach to produce the  $\alpha$ -MnS. XRD pattern of the sample (Figure 8c) demonstrates high crystallinity and is highly indexed to the  $\alpha$ -MnS phase, which has a lattice constant of 5.224 Å (JCPDS 06–0518). The (111), (200), (220), (311), (222), (400), and (420) planes of the  $\alpha$ -MnS are responsible for all of the diffraction peaks at angles of 29.6°, 34.3°, 49.3°, 58.6°, 61.4°, 72.3°, and 82.6°, respectively. The manufactured ZIMBs achieved a high areal capacity of 178 Ah/cm<sup>2</sup>, a specific energy of up to 322 Wh/cm<sup>2</sup>, and a specific power of 120 W/cm<sup>2</sup>. These characteristics made it possible to directly power various devices, including pressure sensors, LEDs, and digital clocks. Engraving allows for the preparation of self-adhesive soft templates with a variety of designs, which can then be put on a variety of substrates in manufacturing MBs. For instance, a template consisting of a pattern of "HNU" characters was created and used to fabricate three ZIMBs on a polyethylene terephthalate (PET) substrate. As a result, a green LED was successfully illuminated (Figure 8d). All of the completed ZIMBs, which come in various forms and sizes, were suitable for use in power electronics. Figure 8(e) shows the performance test of MBs by connecting a pressure sensor to a single ZIMB. The result demonstrated that the sensor functions appropriately and provides transparent relationships between the input pressures and the output currents. Furthermore, the manufactured ZIMB's steady voltage output was inferred from its consistent current output under pressure.

Jin's team<sup>[83]</sup> successfully fabricated solid-state ultra-high capacity and highly reversible ZIMBs through a 3D printed design, enabling seamless wearable integration. The cathode was constructed using calcium vanadium oxide (CaVO) nanorod and the anode was constructed using rGO nanosheet based, which were both fabricated using digital inkjet printing in interdigital patterns to create 3D printed solid-state ZIMBs, as shown in Figure 8(f). The DIW procedure involved loading ink into a syringe, extruding it through nozzles using compressed air, and depositing it onto a target substrate. These 3D-printed inks also benefited from adding acetylene black nanoparticles and CNTs to improve their overall structural integrity (Figure 8g). Before inserting CaVO and rGO with direct current (DC), a silver-based interdigital pattern was pre-printed using the same technique with silver-based inks; this silver-based pattern then solidified and served as the current collector. The DIW technique's superior capability in digitally controlling the pattern of deposited 3D printable inks allowed for the deposition of CaVO NR-based cathode and rGO NS-based anode host onto opposite sides of an interdigital current collector pattern, each side containing a different combination of nanomaterials of various dimensions. The extruded rGO NS-based finger used as the anode host was also designed digitally. It was hypothesized that the rGO NS-based anode host provided a suitable environment for developing Zn NSs, as evidenced by its rough surface. As can be observed in Figure 8(h), NS existed throughout the electrodeposition process, which was tuned by adding Cu to the electrolyte. Symmetric ZIMBs were printed using the same 3D printing

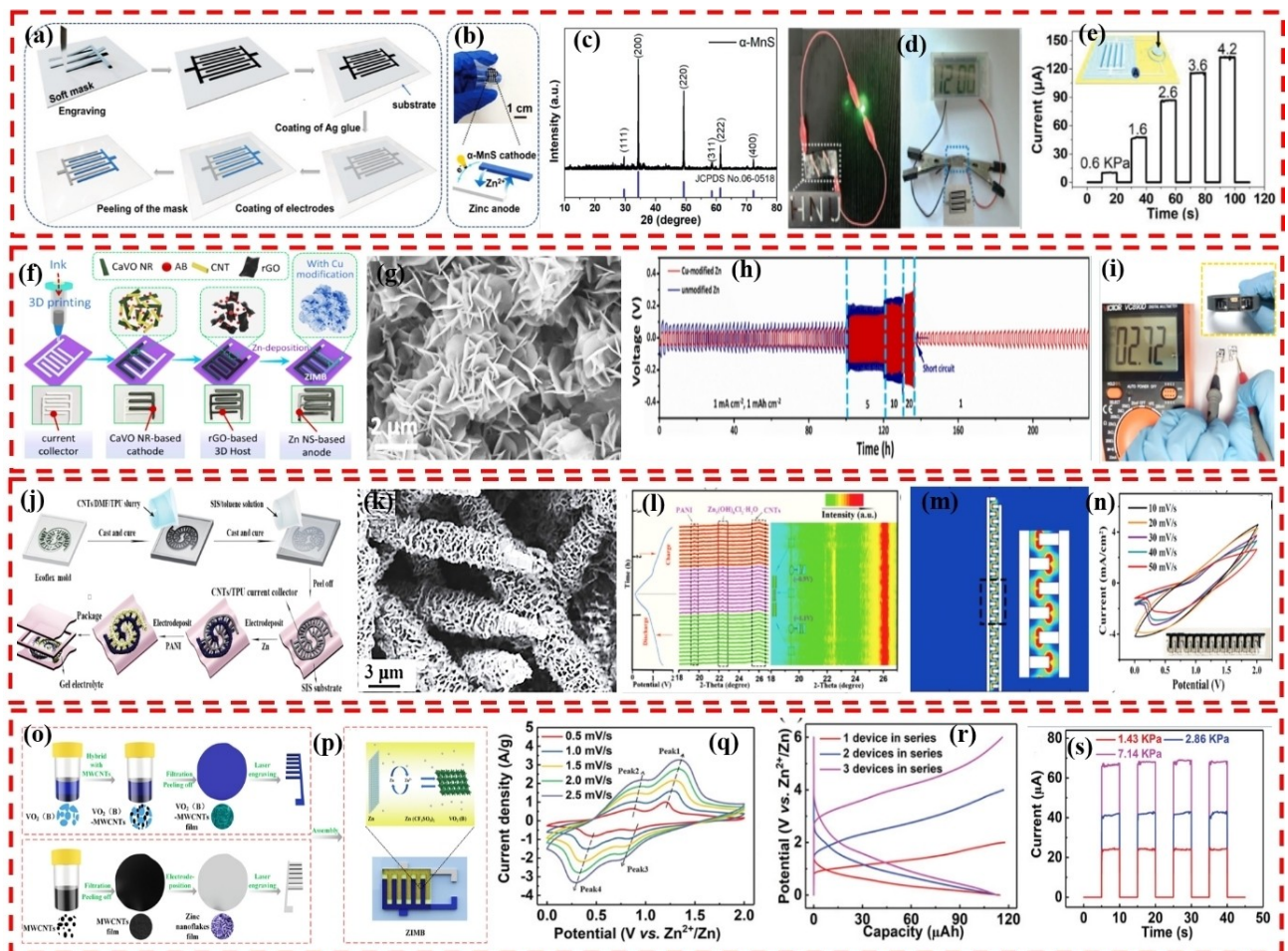


**Figure 8.** a) Schematic representation of soft template engraving and ZIMB fabrications, b) fabricated interdigital ZIMB, c) XRD patterns, d) ZIMBs powering a green LED and a digital clock, e) single ZIMB powdered pressure sensor output currents at various loads. Reproduced with permission from Ref. [82]. Copyright (2021) Wiley. f) Schematic of ZIMB 3D printing process and associated photographs of 3D printed ZIMB, g) SEM image, h) evaluate Cu-modified Zn vs. unmodified Zn symmetric microcells at various current densities, i) two 3DP-CaVO batteries in series showing cell voltage with inset shows digital photo displays printed bracelet with ZIMBs and LED. Reproduced with permission from Ref. [83]. Copyright (2022) Wiley. j) An illustration of the synthesis of concentric circle Zn-PANI MB, k) SEM image of n@CNTs/TPU composite electrode, l) PANI/CNTs@TPU electrode structure and peak intensity contour plots during charge-discharge cycling, m) straight interdigital potential, electric field, and energy simulations, n) CV curves of Zn-PANI MBs with interdigital. Reproduced with permission from Ref. [84]. Copyright (2020) Wiley. The manufacturing procedure of free-standing o)  $\text{VO}_2$  (B)-MWNTs cathode and zinc nanoflakes anode, p) ZIMB's structure and functioning principle, q) CV curves, r) series-connected GCD curves of many ZIMBs, s) Relationships between current and time of the PS driven by one ZIMB in repeated compression-release cycles under different stress conditions. Reproduced with permission from Ref. [85]. Copyright (2019) Wiley.

method to study the electrochemical impact of Cu modification on Zn anodes. The rate performance of Zn symmetric microcells was measured at 1, 5, 10, and 20  $\text{mA}/\text{cm}^2$  at 1  $\text{mAh}/\text{cm}^2$ ; the results are shown in Figure 8(i). At varying current densities, the Cu-modified Zn anode was observed to have lower polarization and more stable Zn plating/stripping than the unmodified Zn anode. Two-finger interdigital microelectrodes were pre-printed onto elastic PET substrates to demonstrate this. Two identical 3D printed ZIMBs were connected in series and coated with PVA Zn ( $\text{CF}_3\text{SO}_3$ )<sub>2</sub> gel electrolyte, demonstrating a consistent and reasonable operating voltage of 2.72 V. LED lighting in rectangular cans was constructed using copper wire and silver paste, and two interdigital ZIMBs were placed inside. Bracelets powered by ZIMBs were successfully fabricated after the cover lids were compressed, showcasing the compatibility of the two

3D printing methods and the enormous potential for wearable energy applications.

Chen's group<sup>[84]</sup> described an in-plane Zn-PANI MB which is flexible and completely solid-state. This ZIMB has a concentric circular topology. To achieve this, cathodes and anodes were electrodeposited directly onto a styrene-isoprene-styrene (SIS) rubber substrate. As described in Figure 8(j), the 3D printing and subsequent electro-deposition operations were used to create the planar Zn-PANI MB with the concentric circular structure. In a nutshell, a 3D printer was used to create the convex concentric-circle structure of the resin slot mould. Nanorods of PANI and Zn micro-rods were electrodeposited directly onto the mould. Zn-PANI MBs were made to be flexible by first being filled with a gel electrolyte and then being packed in a flexible SIS film. The SEM represented the porous structure of the rod-like Zn anode in Figure 8(k). The anode had

a diameter of approximately  $\sim 3 \mu\text{m}$ , a length of approximately  $\sim 10 \mu\text{m}$ , and a thickness of approximately  $\sim 2.0 \mu\text{m}$ . It was also determined that the mass loading of the zinc layer was around  $\sim 0.9 \text{ mg}$ . PANI@CNTs/TPU electrode was investigated by *in situ* XRD technique during the first charge/discharge cycle to investigate the electrochemical mechanism further. The results of this analysis are depicted in Figure 8(l). During the discharge process, the reduction reaction took place on the cathode. There was no visible shift for the characteristic peak of PANI (19.60), demonstrating the exceptional stability of the PANI electrode throughout the first conversion and cycling process. In addition, the characteristic peak in the bi-dimensional contour map steadily shrank as the discharge time increased, signifying the better PANI electrode crystallinity as the reduction reaction was taking place. Energy distributions at the electrodes are also demonstrated in (Figure 8m), with the specific energy increasing as the color changed from blue to red in the simulation results. As a result, a concentric circle-shaped electrode produced far more expansive regions of high energy. CV curves of three distinct types of MBs at 10–50 mV/s are shown in Figure 8(n). The theoretical simulation results agreed with the experimental findings that the Zn-PANI MB with a higher integral area, provided superior battery performance. The MBs have great potential as a suitable power source for next-generation multifunctional wearable devices.

Using a vanadium dioxide (B)-multiwalled carbon nanotubes ( $\text{VO}_2$  (B)-MWCNTs) cathode, a zinc nanoflakes anode, and a zinc trifluoro methane sulfonate-polyvinyl alcohol ( $\text{Zn}(\text{CF}_3\text{SO}_3)_2\text{-PVA}$ ) hydrogel electrolyte, Shi et al.<sup>[85]</sup> described a low cost quasi-solid-state aqueous ZIMBs. (Figures 8o and p) depicts the steps required to fabricate a cathode composed of free-standing  $\text{VO}_2$  (B)-MWCNT “fingers” and an anode comprising Zn nanoflakes. To begin, the zinc nanoflakes and  $\text{VO}_2$  (B)-MWCNTs electrodes were made using a number of procedures, including vacuum filtering, peeling off, and electroplating. Second, the laser engraving equipment was used to directly cut the free-standing films into a finger shape for the  $\text{VO}_2$  (B)-MWCNTs cathode and the Zn nanoflakes anode. The Zn ( $\text{CF}_3\text{SO}_3$ )<sub>2</sub>-PVA hydrogel coating was applied to the polydimethylsiloxane (PDMS) film after the finger-like  $\text{VO}_2$  (B)-MWCNTs cathode and Zn nanoflakes anode were transferred. On the cathode,  $\text{Zn}^{2+}$  was adsorbed and become entrenched. During the charging process, the Zn ( $\text{CF}_3\text{SO}_3$ )<sub>2</sub>-PVA electrolyte was recharged by cycling anions back from the anode to the cathode. At the same time, Zn was synthesized at the anode from  $\text{Zn}^{2+}$  and transported from the cathode via a Zn ( $\text{CF}_3\text{SO}_3$ )<sub>2</sub>-PVA hydrogel electrolyte. Figure 8(q) shows the CV curves of  $\text{VO}_2$  (B)-MWCNTs electrode, which displays two sets of large redox peaks (the anode peaks at 0.869/1.206 to 0.920/1.360 V, and the cathode peaks at 0.873/0.480 to 0.731/0.280 V). The presence of these separation peaks indicated multiple intercalations and deintercalation steps. When the scan rate increases, there is little change in the positions of the peaks at both the anode and cathode. ZIMB's GCD curves in series and parallel connections (Figure 8r). Because each ZIMB has its performance characteristics, the total capacity of several ZIMBs linked in series or parallel will always be just a little bit lower than the theoretical

value. Two or three ZIMBs linked in series have voltage windows about double or triple of a single ZIMB. Also, the capacity of a parallel connection of two or three ZIMBs is twice as high as that of a single ZIMB. Figure 8(s) depicts the time-current relationships of the PS driven by a single ZIMB at varying pressures and driven by a sequence of ZIMBs at a fixed pressure. When specified pressure is given to the PS, the current is doubled or tripled when powered by two or three ZIMBs, respectively. These findings suggest that the ZIMB can be a reliable energy storage device capable of consistently supplying power to other electronic devices.

### 3.2.4. Other micro-batteries

Wang et al.<sup>[86]</sup> proposed a novel fabrication technique, known as transform printing, to create zinc/manganese dioxide in-plane MBs. This method merges 3D printing with metal film stamping to produce intricate metal patterns. The process begins with 3D printing stamps from resin, which are then coated with a thin layer of catalytic ink containing glycerol and  $(\text{NH}_4)_2\text{PdCl}_4$ . These inked stamps are then placed on flexible substrates and pressure is applied to transfer the patterns onto the substrate. Finally, the substrate is soaked in an electroless deposition (ELD) solution of Ni and Au to deposit the metal as shown in Figure 9(a). This method has several advantages over traditional stamp fabrication techniques such as photolithography, including speed and cost-effectiveness. The team used CAD software to create a series of interdigital patterns, to maintain consistent finger width while varying finger spacing. The final product shows high specific energy, low cost, and mechanical flexibility, making them suitable for wearable energy storage devices. The process for creating flexible zinc/manganese dioxide IMBs is depicted in Figure 9(b), along with the overall layout of the finished product. This process involves the electrochemical deposition of zinc metal on one side of the Au/Ni interdigital fingers, which serves as the anode, following the pattern of the Au/Ni current collector on the flexible substrate. The interdigital phalanges are located on this side of the flexible substrate. Conversely, manganese dioxide is deposited across the fingers' interspaces using an electrochemical method. Electro deposition was chosen for this application due to its low environmental impact, lack of need for polymer binders, and manageable reaction temperatures. A PVA gel electrolyte containing  $\text{ZnSO}_4$  and  $\text{MnSO}_4$  was applied using a drop-coating technique to complete the  $\text{Zn}/\text{MnO}_2$  interdigital membrane biosensor assembly. This method is simple, and effective, providing great design flexibility when preparing flexible  $\text{Zn}/\text{MnO}_2$  in-plane. Figure 9(c) shows the XRD pattern, which exhibits visible diffraction peaks characteristic of the normal Zn phase (PDF # 04-0831), while the amorphous phase of the electrodeposited  $\text{MnO}_2$  materials does not exhibit any such peak. SEM images of the electrode (Figure 9d) further illustrate the uniform coating of  $\text{MnO}_2$  (10 nm) and Zn metal (15 nm), both of which have a dense coating. The Au/Ni composite is characterized by a uniform coating of  $\text{MnO}_2$

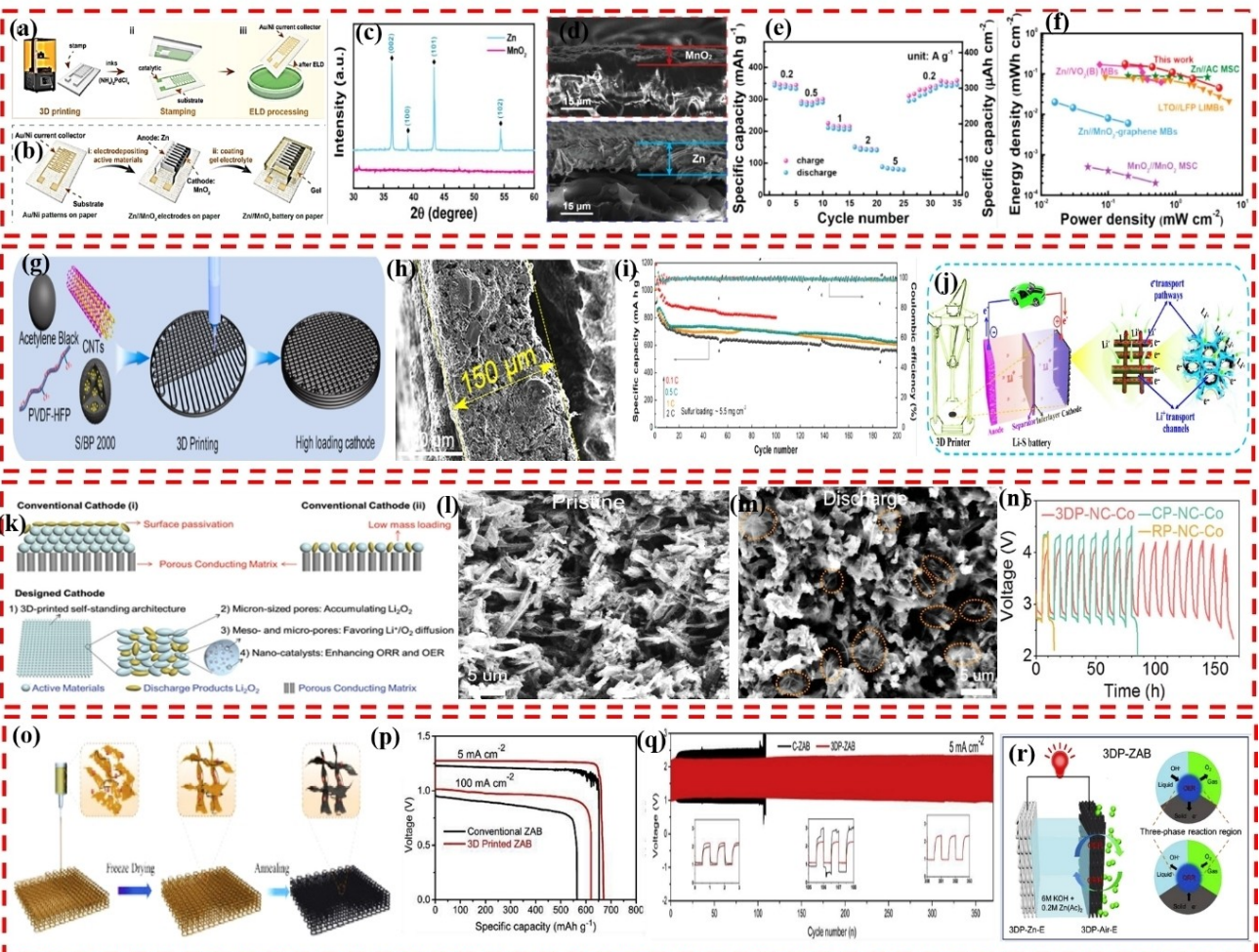


**Figure 9.** a) Schematic representation of the manufacturing process of a 2D metal design and an in-plane Zn//MnO<sub>2</sub> MB, b) Zn//MnO<sub>2</sub> MB fabrication on filter paper, and its corresponding c) XRD patterns, d) cross-sectional SEM image, e) rate performance, and f) Ragone plot. Reproduced with permission from Ref. [86]. Copyright (2022) Elsevier. (g) Schematic of 3D printed S/BP 2000 thick cathodes (diameter of grid electrode: 10 mm), h) cross-sectional SEM image of one and four-layer 3D printed cathodes, respectively, i) cycling stability of Li–S battery, j) 3DP-FDE in Li–S batteries provides outstanding micro-and nano-scale Li<sup>+</sup>/e<sup>-</sup> transport. Reproduced with permission from Ref. [87]. Copyright (2019) Elsevier. k) Model comparison of three different Li–O<sub>2</sub> cathodes for Li<sub>2</sub>O<sub>2</sub> coating, l) cross-sectional SEM image of 3DP-NC-Co, m) SEM image after discharge current density of 0.05 mA/cm<sup>2</sup>, and n) cycle stability using the designated cathodes with a 1 mAh capacity cap and 0.1 mA/cm<sup>2</sup>. Reproduced with permission from Ref. [88]. Copyright (2018) Wiley. o) Schematic diagram of 3DP–Zn–E and 3DP–Air, and the corresponding p) galvanostatic discharge curves, q) cycling stability. r) An illustrated diagram of 3DP-ZAB's, and the reaction region of 3DP-ZAB. Reproduced with permission from Ref. [81c]. Copyright (2020) Elsevier.

(10 nm) and Zn metal (15 nm), both of which exhibit a dense coating.

Figure 9(e) illustrates the rate performance of Zn/MnO<sub>2</sub> metal-based SC at current densities of 0.2, 0.5, 1.0, 2.0, and 5.0 A/g. The results show that the final gravitational specific capacities are 336, 282, 208, 146, and 85 mAh/g, corresponding to areal specific capacities of 304, 253, 183, 128, and 74 Ah/cm<sup>2</sup>. Notably, the battery's specific capacity returns to its initial value after being rapidly discharged from 5 A/g to 0.2 A/g, indicating high electrochemical stability and reversibility of charge and discharge. Additionally, Zn/MnO<sub>2</sub> IMBs demonstrate high specific energy of 168 Wh/cm<sup>2</sup> at a specific power of 0.18 mW/cm<sup>2</sup> and 4.5 mW/cm<sup>2</sup> at a specific energy of 43 Wh/cm<sup>2</sup> in the aqueous electrolyte (Figure 9f). Using gel-state IMBs also demonstrates mechanical pliability at a range of bending angles. Given their excellent specific energy, low cost, and

mechanical flexibility, aqueous Zn/MnO<sub>2</sub> IMBs have the potential to serve as the primary form of an energy storage device in the emerging market for flexible and wearable electronics in the future. Further research is necessary to identify the optimal balance between performance, material availability, and scalable fabrication methods.

Gao et al.<sup>[87]</sup> have reported the successful 3D printing of high-specific energy and specific-power sulfur/carbon cathodes for Li–S batteries. The fabrication process of the S/BP-2000 electrode, as illustrated in Figure 9(g), involves three main steps: (1) ink preparation, (2) 3D printing, and (3) post-treatment (phase inversion and freeze-drying). The ink is prepared by dissolving a PVDF-HFP solution containing 1-methyl-2-pyrrolidinone (NMP) as a solvent, which is used to disperse the S/BP-2000 composite with conductive additives such as CNTs and acetylene black. The ink was then loaded into

a syringe and operated by a 3D printer to create the desired structure. The printed electrode is then subjected to freeze-drying to remove the solvent from the ink, resulting in a freestanding, bendable sulfur cathode. A cross-sectional image of the printed cathode, as shown in Figure 9(h), reveals that a single printed layer has a thickness of 150 nm, corresponding to a sulfur loading of 1.3–1.5 mg/cm<sup>2</sup>. The cyclability of the 3D printed cathode (3DP-FDE) with a sulfur loading of 5.5 mg/cm<sup>2</sup> was investigated at various current densities (0.1 C, 0.5 C, 1 C, and 2 C). The cell exhibits a high initial capacity of 1188 mA h/g at 0.1 C, as shown in Figure 9(i). After a rapid drop in capacity at the initial cycles, the cell reaches its reversible capacity of 926 mA h/g in the seventh cycle. The battery maintains its high capacity of 802.4 mA h/g even after being cycled one hundred times, indicating the battery's remarkable cycling stability, with a capacity attenuation rate of only 0.14% per cycle (estimated based on the 7th cycle). The good cycle stability of the 3DP-FDE with high sulfur loading is attributed to the increased ionic and electrical conductivity of the cathode by the 3D printing fabrication method. The printed cathode features a macro-scale grid pattern optimized for Li<sup>+</sup>/e<sup>-</sup> transport, increasing surface area and thus maximizing sulfur utilization and discharge capacity. In addition, the macropores of the grid structure, the micropores in BP-2000, and the nanopores generated during phase inversion of the binder anchor the well-located polysulfides in the cathode, lowering the shuttling effect and increasing the cycle stability Figure 9(j). The study opens up new possibilities for constructing Li–S batteries with high energy and power densities based on 3D printing technology. It also sheds light on the development of other energy storage devices such as Li-ion and Li–O<sub>2</sub> batteries.

Lyu et al.<sup>[88]</sup> demonstrated the ability to create a hierarchically porous carbon framework containing embedded Co nanoparticles by 3D printing a cobalt-based metal-organic framework (Co-MOF) with an extrusion-based printer and then annealing it appropriately. A significant contributor to the overall decrease in specific energy use is the suitable cathode catalysts to support the Li<sub>2</sub>O<sub>2</sub> product. The preparation of the cathode can be divided into two groups of conventional methods: (1) coating powdered catalyst onto a porous conducting matrix (such as carbon paper, carbon cloth, and nickel foam) and (2) directly growing the catalysts on the matrix (Figure 9k). SEM images before and after discharge (Figure 9l and m) show the printed filament in the 3DP-NC–Co cathode, with the possible microporous structures within the filament promoting further deposition of Li<sub>2</sub>O<sub>2</sub>. A large discrepancy in specific capability becomes apparent when the enabling matrix is considered. The 3DP-NC–Co cathode, with only 1 mAh storage and a current density of 0.1 mA/cm<sup>2</sup>, has a much lower overpotential and higher cycle ability than RP-NC–Co and CP-NC–Co (Figure 9n). This hierarchically porous network increases discharge capacity through the confinement of micro-scale pores and Co-based catalysis in the mesoporous carbon flakes, which promotes the efficient deposition of Li<sub>2</sub>O<sub>2</sub> particles and facilitates the decomposition of insulating Li<sub>2</sub>O<sub>2</sub>. As a result, once the porous matrix was pushed toward a self-standing catalyst design, the practical specific energy of the cell

was greatly increased, reaching a high value of 798 Wh/kg. This study suggests positive implications for using 3D printing as a technique in developing superior battery systems, by demonstrating a novel approach to the design and integration of MOF-derived carbon-based nanomaterials into a self-standing hierarchical porous architecture.

Zhang et al.<sup>[81c]</sup> presented a 3D printing technique for fabricating functioning zinc-air battery (ZAB) electrodes (containing anode and cathode). The printing technique was used to synthesize functioning electrodes successfully for ZAB. Zn powder, carbon black, and various chemicals are included in the ink used to print the anode directly. Figure 9(o) depicts the procedure for the fabrication of the cathode. This process includes printing, freeze-drying, and annealing. The high level of Zn usage was made possible because of the porous anode, which comprises numerous Zn microspheres. The 3D-printed air cathode possesses a high surface area and hierarchical porous structure, imparting high electrocatalytic activity and a rapid diffusion channel for the reaction. As a result, the 3D printed zinc-air batteries (3DP-ZABs) demonstrate higher specific capacity and higher cycling stability than those of the capacities of 3D printed ZABs are higher than those of C-ZABs, particularly at high discharge current densities, with capacities of 651 and 564 mA h/g at 5 and 100 mA/cm<sup>2</sup>, respectively, normalized to the mass of consumed zinc. Additionally, 3DP-ZABs have a fast dynamic response and good rate capabilities at various current densities (Figure 9p). The solid-state 3D-printed ZABs also maintain a steady discharge and charge cycle at 1 mA/cm<sup>2</sup> throughout their operation (Figure 9q). However, after 200 cycles, the performance of the quick solid-state 3DP-ZAB battery shows a slight decrease in terms of the large charge voltage and low discharge voltage plateaus, due to the loss of water from the gel-like electrolyte, which reduces its ionic conductivity. The features of the prepared 3D-printed ZABs and C-ZABs are shown schematically (Figure 9r). This work demonstrated the feasibility of printing battery electrodes, which has the potential to revolutionize battery production by providing a new method for producing high-performance batteries with improved specific capacity, cycling stability, and rate capabilities.

The 3D printing techniques utilized in the fabrication of electrode materials for MIMBs include stereolithography, electrodeposition, 3D printing, and stampings, engraving soft templates, and powder bed fusion. The SLA technique offers high resolution, superior surface finish, and efficient production of prototypes or small-scale runs of fabrication of micro-electrochemical devices also capable of printing complex structures. However, SLA has limitations in multi-material deposition selection, and its printed objects may be brittle, increasing the risk of breakage or damage. Size limitations are also a factor to consider. Aerogel jet printing enables the creation of intricate and precise electrode structures with material versatility. It allows for the fabrication of electrodes with tailored geometries to meet specific performance requirements. On the other hand, time-consuming and high-cost fabrication is another drawback of this technique. Electrodeposition is advantageous for its excellent conductivity and

suitability for large-scale production at a lower cost. However, it is limited in complexity, has surface roughness issues, and requires control of electrode thickness. The 3D Printing and Stampings technique offer design flexibility, rapid prototyping, and a wide range of conductive materials. Additionally, it has limitations in poor precision, is relatively expensive, and may require post-processing for surface finish and conductivity enhancement. Engraving Soft Template is compatible with various conductive materials, offering high precision and scalability for mass production. On the other hand, it has limitations in complexity and can generate material waste. Powder bed fusion exhibits merits based on its material versatility, design flexibility, batch production, and reduced material waste. However, it comes with a higher equipment cost, limited build volume, process complexity, and surface roughness challenges.

### 3.3. Metal-ion hybrid micro-supercapacitors

#### 3.3.1. Sodium-ion hybrid micro-supercapacitors

MIHMSCs have a battery-style anode and a capacitor-style cathode to deliver greater specific power density than batteries. The combination can notably improve the voltage window and electrochemical performance of hybrid devices.<sup>[89]</sup> Na-ion hybrid micro-supercapacitors (NIHMSCs) with an AC cathode and a nitrogen-doped MXene ( $N\text{-Ti}_3\text{C}_2\text{T}_x$ ) anode were reported by Fan et al.<sup>[90]</sup> In Figure 10(a), a simplified illustration of the processes involved in 3D printing an  $N\text{-Ti}_3\text{C}_2\text{T}_x$  electrode in a woodpile configuration is described. Then, using melamine formaldehyde (MF) nanospheres as a starting point for the synthesis, porous  $N\text{-Ti}_3\text{C}_2\text{T}_x$  was created using a sacrificial templating approach. Exfoliated  $\text{Ti}_3\text{C}_2\text{T}_x$  sheets have a negative charge due to the presence of hydroxyl (OH) and carbonyl (COOH) groups on their surfaces, while MF spheres have a

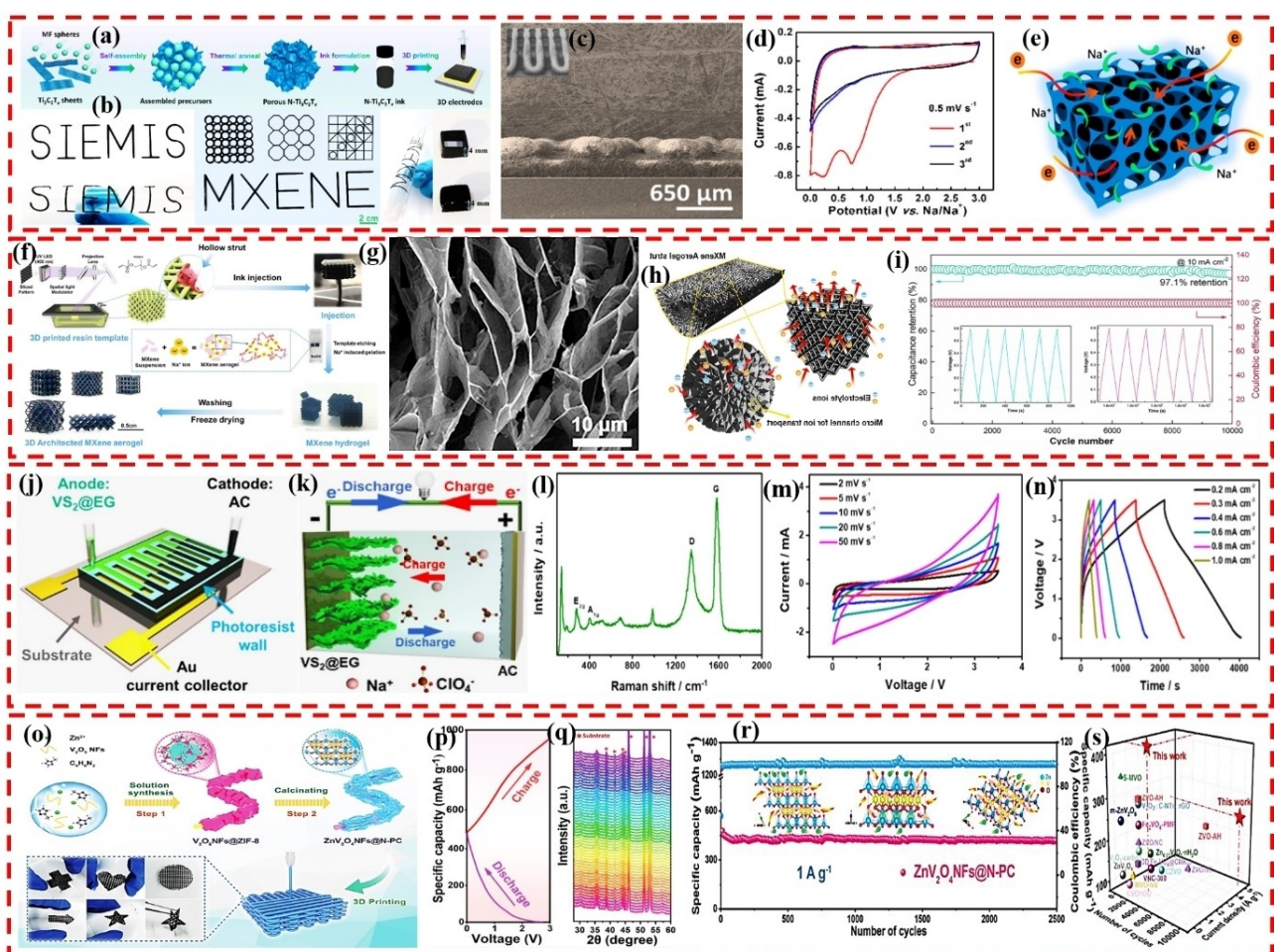


**Figure 10.** a) Schematic of 3D printed porous  $N\text{-Ti}_3\text{C}_2\text{T}_x$  electrodes from MF sphere template. b) 2D geometric patterns and 3D freestanding constructions printed using  $N\text{-Ti}_3\text{C}_2\text{T}_x$  ink, c) SEM image, d) CVs, e) Schematic illustration of  $\text{Na}^+$  and electron transport. Reproduced with permission from Ref. [90]. Copyright (2020) American Chemical Society. f) Schematic diagram of 3D printed MXene, g) SEM image. h) Schematic of a 3D Na-MXene electrode with low tortuosity and enough ion migrations. i) Long-term stability of 3D Na-MXene. The inset shows initial and final charge/discharge curves. Reproduced with permission from Ref. [91]. Copyright (2022) American Chemical Society. j) Schematic diagram of non-aqueous NIHMSCs based on  $\text{VS}_2\text{@EG}$ , k) working mechanisms, l) Raman spectrum of  $\text{VS}_2\text{@EG}$ , m) CVs of NIHMSCs, n) GCDs of NIHMSCs. Reproduced with permission from Ref. [89b]. Copyright (2019) Wiley. o) Synthesis technique and 3D printed  $\text{ZnV}_2\text{O}_4\text{NFs}@N\text{-PC}$  patterns, p) charge/discharge curve at 0.1 A/g, q) *in-situ* XRD, r) cycling stability, s)  $\text{ZnV}_2\text{O}_4\text{NFs}@N\text{-PC}$ 's long-life cycle compared with V-based materials. Reproduced with permission from Ref. [92]. Copyright (2022) Wiley.

positive charge due to the capture of a proton ( $H^+$ ) from the solution by nitrogen-containing groups ( $NH_2$ ) on their surfaces. Digital images of as-printed designs on a polyethylene terephthalate substrate, such as those labeled "SIEMIS" and "MXENE," also show the designs' high degree of flexibility and adaptability.

Two freestanding structures, each with a height of roughly 4 mm, were fabricated using N-Ti<sub>3</sub>C<sub>2</sub>T<sub>x</sub>-ink and a specially designed printing program (Figure 10b). This indicates that 3D printing is a great method for making large and heavy-loading electrodes. Such 3D-printed electrodes were perfectly cemented by vacuum cyro-drying while retaining their internal architecture. To the side, the resulting N-Ti<sub>3</sub>C<sub>2</sub>T<sub>x</sub> electrodes resemble neat stacks of wood (Figure 10c), with no sign of internal collapse at the boundary between the different filament layers. Based on these results, it is clear that 3D printing electrodes with stable configurations require high-quality modulated inks. Na metal was used for both the counter and reference electrodes in a prototype coin cell to examine further the electrochemical performance of the resulting N-Ti<sub>3</sub>C<sub>2</sub>T<sub>x</sub> samples for Na-ion storage. The typical N-first Ti<sub>3</sub>C<sub>2</sub>T<sub>x</sub>'s three CV cycles against Na/Na<sup>+</sup> at a potential range of (0.01–3.0 V) and a rate of 0.5 mV/s are shown in Figure 10(d). Consistent with the low Coulombic efficiency in the initial charge-discharge curves, an irreversible cathodic peak was likely caused by the solid electrolyte interphase formation during the electrochemical reaction. In the subsequent two CV scans, cathodic and anodic signals at 0.6/0.8 V, correspond to the reversible Na<sup>+</sup> insertion/extraction in N-Ti<sub>3</sub>C<sub>2</sub>T<sub>x</sub>. Figure 10(e) shows the rationally developed electrode structures for Na-ion storage. Interconnected Ti<sub>3</sub>C<sub>2</sub>T<sub>x</sub> nanosheets have a porous structure and excellent electrical conductivity, creating multi-dimensional ion routes that decrease ion diffusion length. Small pores ensure excellent electrolyte penetration and interface reaction efficiency, speeding up electrochemical reactions. Porous N-Ti<sub>3</sub>C<sub>2</sub>T<sub>x</sub> with high conductivity and an easy ion diffusion route can be employed as the anode of NIHMSCs to provide excellent electrochemical performance. Finally, the improved NIHMSC has a specific energy/specific power of 101.6 Wh/kg and 3269 W/kg, which is superior to many MSCs and MBs.

Qiu's group<sup>[91]</sup> demonstrated a novel method for producing additive-free 3D architected MXene aerogels through a 3D printed template-assisted approach (Figure 10f). This method combines a DLP 3D printer to design a sophisticated 3D resin template with a resolution of 10  $\mu$ m, and a cation-induced gelation process (Figure 10g). The additive-free aqueous MXene ink is injected into the template's hollow struts, followed by O<sub>2</sub> plasma treatment, and immersion in NaOH, leading to the cross-linking of MXene nanosheets into a 3D hydrogel network. The hydrogel is then freeze-dried, resulting in a lattice structure with microcellular microstructure. Electrochemical evaluations were conducted to determine the capacitance of the 3D Na-MXene and to investigate the influence of the 3D structure on charge storage properties in Figure 10(h). The results indicated that the 3D Na-MXene aerogel exhibits a high areal capacitance of 7.5 F/cm<sup>2</sup> and maintains stability, retaining 97.1 % of its initial

capacitance after 10,000 GCD cycles (Figure 10i). Furthermore, the 3D lattice structures in this approach allow for the optimization of the tortuosity of electrodes, enhancing ion diffusion, thus making this technique a valuable tool for improving the performance of energy storage materials.

Feng's group<sup>[89b]</sup> demonstrated a new kind of non-aqueous NIHMSC. VS<sub>2</sub> nanosheets grown on electrochemically exfoliated graphene (VS<sub>2</sub>@EG) were as an anode, and AC as a cathode, in a non-aqueous sodium-ion electrolyte. The asymmetric construction and working mechanism of non-aqueous NaClO<sub>4</sub> dispersion NIHMSCs are shown schematically in Figure 10(j and k), and are achieved by moving a slurry of VS<sub>2</sub>@EG (or AC), binder, and acetylene black into the pre-designed micro-channels. In a NaClO<sub>4</sub>-based organic electrolyte, VS<sub>2</sub>@EG and AC electrodes were used to construct the NIHMSC. The Raman spectrum of VS<sub>2</sub>@EG, as depicted in Figure 10(l), illustrates the presence of the E<sub>2g</sub> and A<sub>1g</sub> vibration modes of VS<sub>2</sub>, and D and G bands of EG. Achieving a high-efficiency level was facilitated by maintaining a balanced mass ratio between these two electrodes. By examining the electrochemical behavior of the VS<sub>2</sub>@EG anode and AC cathode against a Na foil in half cells, it was determined that the optimal mass ratio of AC/VS<sub>2</sub>@EG falls within the range of 3.4–4.0. Typically, the combined mass of a VS<sub>2</sub>@EG anode and an AC cathode is approximately 3 mg, as illustrated in Figure 10(k). The non-aqueous NIHMSC demonstrated a high voltage of 3.5 V, as shown in Figure 10(m). The GCDs at different current densities are depicted in Figure 10(n) and exhibit a pseudocapacitive charge storage behavior characterized by asymmetrical forms. The non-aqueous NIHMSC exhibited remarkable areal capacitance of 110.7 mF/cm<sup>2</sup> after completing a single charge-discharge cycle, which took 2400 seconds to be completed at a current density of 0.2 mA/cm<sup>2</sup>. Such studies not only promote the advancement of miniature energy storage devices but also suggest a significant potential for future self-powered electronics development.

According to the results reported by Yuan et al.,<sup>[92]</sup> a 1D core-shell structure composed of N-doped porous carbon encapsulating ZnV<sub>2</sub>O<sub>4</sub> nanofibers (ZnV<sub>2</sub>O<sub>4</sub> NFs@N-PC) can be fabricated. This structure exhibits an open framework and favorable properties that enhance ion diffusion, mass transportation, and electron transfer, making it an effective material for Na<sup>+</sup> storage. The ZnV<sub>2</sub>O<sub>4</sub>NFs@N-PC was synthesized using the procedure outlined in Figure 10(o). By utilizing in situ XRD to confirm the structural development of ZnV<sub>2</sub>O<sub>4</sub>NFs@N-PC during the cycling process, it is possible to demonstrate that the ZnV<sub>2</sub>O<sub>4</sub>'s diffraction peaks are still discernible throughout the entire sodiation and dissociation process (Figure 10p, q). The diffraction peak at 30.26°, which is indicative of the reversible diffusion of Na<sup>+</sup> for ZnV<sub>2</sub>O<sub>4</sub> in the sodium storage process, drops to a lower angle as the discharge progresses and then recovers after a full charging step. The Na<sup>+</sup> intercalation and deintercalation within the ZnV<sub>2</sub>O<sub>4</sub> open framework were responsible for the lattice's expansion and contraction, respectively, as indicated by the peak's modest shift. The effective confinement of ZnV<sub>2</sub>O<sub>4</sub> nanofibers within a multi-porous conductive host may increase the electrochemical

reversibility and durability at high current density for  $\text{ZnV}_2\text{O}_4\text{NFs@N-PC}$  anode by promoting diffusion-dominated redox reactions and remarkably accelerating the  $\text{Na}^+$  diffusion. Furthermore, the cyclic stability of the anode over time at a high current density of 1 A/g was examined (Figure 10r). After 2500 cycles, the  $\text{ZnV}_2\text{O}_4\text{NFs@N-PC}$  electrode still exhibited a capacity of 418.4 mAh/g. Notably, the  $\text{ZnV}_2\text{O}_4\text{NFs@N-PC}$  stands out among previously reported vanadium-based anodes for sodium batteries, providing a steady discharge capacity of roughly 245.8 mAh/g after 10,000 cycles, even at an ultra-high current density of 5 A/g (Figure 10s). Such work will provide a successful method for creating promising electrode materials and present enormous prospects for creating NIHMSCs devices that can be produced commercially.

### 3.3.2. Zinc-ion hybrid micro-supercapacitors

Zinc-ion hybrid supercapacitors (ZIHSCs) have received considerable attention because of their high specific energy/high specific power characteristics since they combine a zinc battery-type anode with a matched capacitor-type cathode. Surmounting the kinetic imbalance between the anode and cathode is the key to high-performance ZIHSCs.<sup>[93]</sup> To achieve this goal, searching for suitable high-capacitance cathode candidates with enhanced  $\text{Zn}^{2+}$  diffusion is a potential solution. Numerous types of porous carbon cathodes are the subject of a significant amount of research and development at this point.<sup>[94]</sup> Sun's group<sup>[95]</sup> revealed that the 3D-printed  $\text{Ti}_3\text{C}_2\text{T}_x$ -MXene cathode demonstrated the high-capacity and long-life ZIHSCs by allowing for optimum carrier transport, simple electrolyte penetration, and sufficient porosity. The "Zn" design here has a height of around 5 mm and was printed in layers using an extrusion-based 3D printing process with MXene ink. In addition, a PET substrate with various shaped tailored frameworks presents a high level of diversity and flexibility. Additionally, the printed topologies allow for the persistence of as-designed characteristics following cryo-drying, which hints at the enormous potential of  $\text{Ti}_3\text{C}_2\text{T}_x$ -MXene ink for the exact creation of freestanding electrodes of current-collector-free energy storage devices (Figure 11a). The XRD patterns were obtained from the 3D-printed MXene electrode and the MXene film (Figure 11b). The decrease in double-layer thickness that  $\text{Zn}^{2+}$  generated might be attributed to the reason for the apparent shift of the (002) peak toward a higher angle in 3D printed MXene electrodes ( $6.2^\circ$ ), as compared with the MXene film ( $5.8^\circ$ ). When a conventional ZIHSC system cycles, Zn is typically stripped/deposited at the anode side (often in the form of Zn plates), which causes the Zn anode to irreversibly consume itself and will result in the creation of infamous Zn dendrites. As a result, the performance of the device would ultimately suffer dramatically. Consequently, ZIHSC complete full cells were designed with 3D printed CNT/Zn as the anode and 3D-printed MXene serving as the cathode, as shown in Figure 11(c). In addition, the 3D printed ZIHSC complete cells have favorable cyclic stability, demonstrating a capacity retention of 86.5% and a Coulombic efficiency of 98% even

after more than 6000 cycles at  $10 \text{ mA/cm}^2$  (Figure 11d). This 3D-printed ZIHSC has the potential to be useful in a variety of real-world settings, as demonstrated by the fact that it can effectively power an electronic clock.

Mattevi's group<sup>[96]</sup> reported an improvement in the capacity and durability of Zinc-Ion (ZIHSCs) by incorporating a hybrid-ion electrolyte with a high-mass-loading 3D printed graphene-carbon nanotube (Gr-C) cathode. The volume and area of the active material could be precisely controlled through a layer-by-layer deposition process (Figure 11e). This allowed the 12-layer structures to achieve a loading roughly 20 times greater than that of thin film electrodes. The electrodes were designed with a tailored architecture that includes periodic channels and large pores between the printed filaments, allowing for a large electroactive area in contact with the electrolyte despite the large mass loading. These characteristics promote electrolyte penetration. SEM image revealed that CNTs cover the surface in the Gr platelets, connecting neighboring platelets, thereby enhancing electron transport in the 3D structure (Figure 11f). As a result, the Gr-C structure has an electrical conductivity that is twice as high as that of bare Gr electrodes ( $8.64 \text{ S/cm}$ ). *Ex-situ* SEM and optical microscope analyses (after plating-stripping tests), as shown in Figure 11(g), highlighted the different cycling behavior of Zn metal in the two electrolytic systems. After repeated cycling in the pure electrolytes, Zn electrodes will form layers of insulating by-products and dead Zn, appearing as lumps and large vertical hexagonal platelets. On the other hand, Zn electrodes recycled in a hybrid electrolyte, look more like a flat foil, with tiny, isolated particles scattered across its surface. The ability to track the rate performance of energy storage devices is crucial, as it determines the devices' viability for high-power, cutting-edge applications. Typically, a range of current densities (I/A) was used for GCD analysis. The gaining rate performance of highly loaded 3D ZIHSC was particularly slow and time-consuming when using the GCD method (Figure 11h). An individual GCD cycle on a 12 L Gr-C/Zn cell took about 15 hours, using a charge-discharge current I/A of  $0.2 \text{ mA/cm}^2$ . At  $3 \text{ mA/cm}^2$ , the 3D Gr-C/Zn cell showed a maximum capacity of  $0.84 \text{ mAh/cm}^2$ , significantly higher than that of the pristine electrolyte-based ZIHSCs ( $0.72 \text{ mA/cm}^2$  and 14.8%). These results open the door to the practical development of high-capacity energy storage devices with efficient electrolytes and highly conductive 3D electrodes at a reasonable cost.

Yu Liu et al.<sup>[97]</sup> utilized a combination of DIW and FDM to establish a process for 3D printing conformable ZIHSCs with hierarchical porous micro lattice cathodes, metal anode stabilizers, quasi-solid gel electrolytes, and plastic containers. As illustrated in Figure 11(i), involves the 3D printing of a porous framework cathode, a graphene stabilizer layer for regulating the zinc metal anode, and a gel electrolyte generated through DIW, as well as a plastic packaging produced using the FDM approach. The 3D printing process is employed to fabricate a graphene-based metal stabilizer on Zn foil, which regulates the Zn deposition process and prevents the formation of Zn dendrites, as shown in Figure 11(j, k). The study further demonstrated that as the number of cells linked in parallel

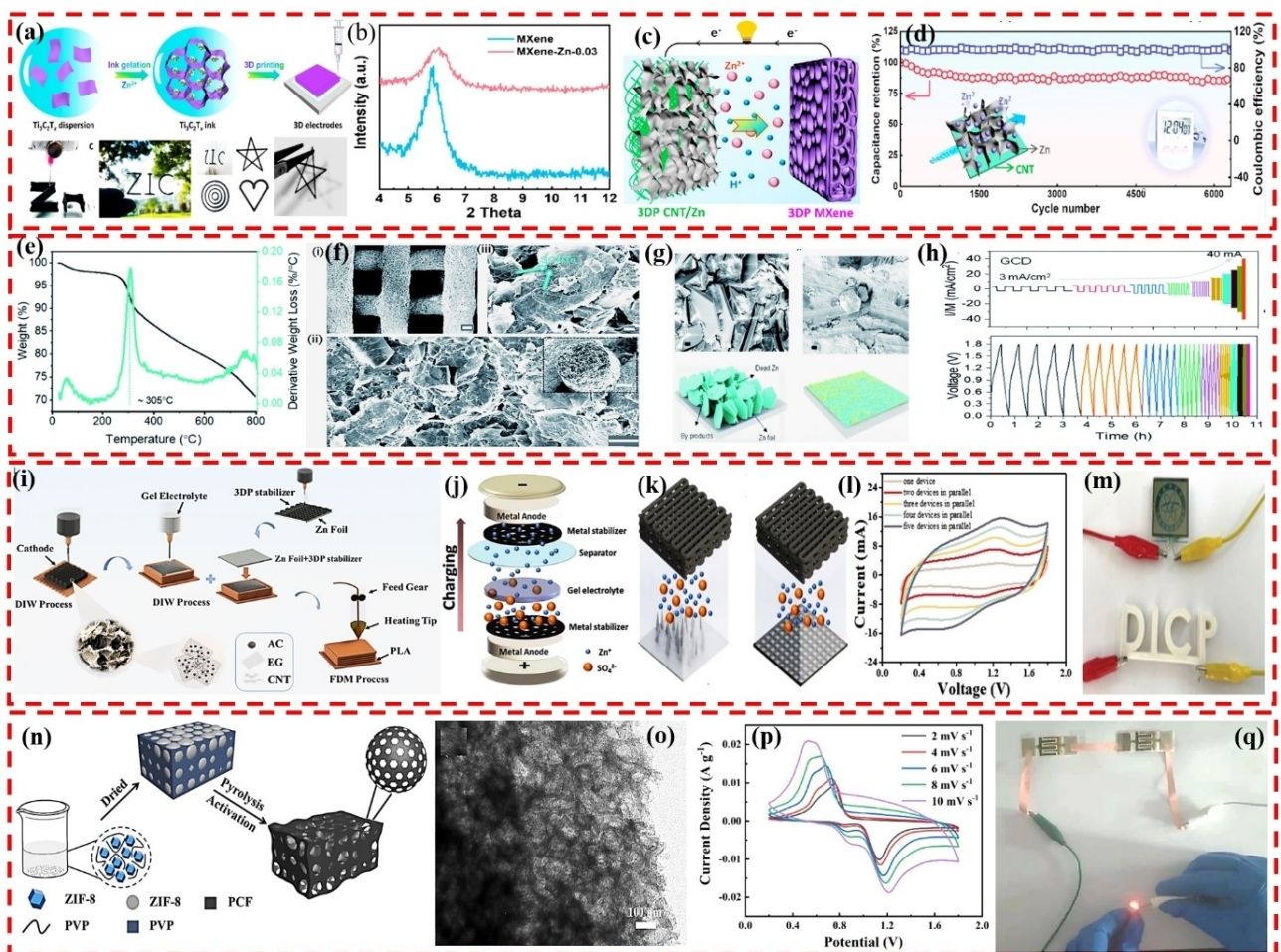


**Figure 11.** a) Schematic illustrating 3D printing via MXene ink and electrodes, digital images of 3D printed architecture and geometric prints from MXene inks, b) XRD patterns 3D printed MXene and pristine MXene suspension, c) illustrating diagram of 3D printed ZIHSC, d) cycling stability. Reproduced with permission from Ref. [95]. Copyright (2021) American Chemical Society. e) TGA and DTA of Gr-C composite versus heating temperature, f) low- and high-magnification SEM images, g) ex-situ SEM images of cycled Zn metal using pure  $ZnSO_4$  and hybrid electrolyte, h) rate measurement results of 3D Gr-C/Zn cells with increasing charge-discharge (bottom and top, respectively). Reproduced with permission from Ref [96]. Copyright (2022) Royal Society of Chemistry. Schematic diagram of i) 3D printed ZIHSCs showing cathode, metal stabilizer, quasi-solid gel electrolyte, and plastic packaging printing, j) 3DP@Zn/3D printed@Zn, k) 3D printed ZIHSCs with/without metal stabilizers layer, l) CV curves, m) digital image of LCD operated by a "DICP"-shaped ZIHSC. Reproduced with permission from Ref. [97]. Copyright (2022) Wiley. n) Schematic depiction of the PCF preparation procedure, o) TEM image, p) CV curves, q) digital images of red LEDs driven in series by two devices. Reproduced with permission from Ref. [98]. Copyright (2021) Wiley.

increases, the current of CV curves (Figure 11l) produced at the same scan rate increases, indicating the exceptional uniformity of 3D-printed ZIHSCs. This highlighted the potential of 3D printed ZIHSCs in integrated circuits, with the ZIHSCs demonstrating a remarkable energy density of  $1514 \mu\text{Wh}/\text{cm}^2$  and an outstanding areal capacitance of  $4259 \text{ mF}/\text{cm}^2$ . Additionally, the ability to create ZIHSCs of various forms and sizes was demonstrated, as the 3D printed ZIHSCs with the "DICP" letter form were able to illuminate an LCD screen displaying the "DICP" logo (Figure 11m).

Gu et al.<sup>[98]</sup> effectively designed a high-performance zinc-ion hybrid micro-supercapacitor (ZIHMSC) using DIW by utilizing hierarchical honeymoon-like porous carbon frameworks (PCFs) as cathodes. As illustrated in Figure 11(n), the formation process involved using a coordination complex of  $Zn^{2+}$  and 2-methylimidazole to form a zeolitic imidazolate framework (ZIF-8) polyhedron. The ZIF-8 particles were then encased in

polyvinylpyrrolidone (PVP) after water vaporization and then converted into a honeycomb-like carbon framework (HCF) through a pyrolysis process that involved removing any remaining KOH with a dilute acid solution. This process increased in the meso and micro-porous structures of the PCF, as can be observed in the TEM image shown in Figure 11(o). The pore size and distribution of the cathode are advantageous for the rapid filtration and diffusion of electrolytes. The electrochemical performance of the direct ink printing ZIHMSCs was then evaluated using CV techniques. Distorted rectangular forms of the CV curves, as displayed in Figure 11(p), highlight the synergistic energy storage mechanisms of  $Zn^{2+}$  insertion/extraction on the anode and reversible ion adsorption/desorption on the cathode. As a result, the printed ZIHMSCs have an excellent specific capacity of  $189.06 \text{ mAh/g}$  at a current density of  $1 \text{ mA}/\text{cm}^2$ , an excellent specific energy of  $76.38 \text{ Wh}/\text{kg}$ , and a specific power of  $499.94 \text{ W}/\text{kg}$ , as well a long-term

cycling stability (capacity retention of 95.71% after 1000 cycles), which outperforms the majority of the state-of-the-art ZIHMSCs. As shown in Figure 11(q), when two serial devices are linked together, a red LED light can be illuminated and maintained for about 5 minutes. Therefore, the device in its current form has promising applications in clean energy storage. Additionally, the stone paper-based printed devices exhibited remarkable mechanical flexibility. The work provides important insight into the creation of feasible next-generation electrochemical energy storage systems.

### 3.3.3. Other metal-ion hybrid micro-supercapacitors

According to Luong et al.,<sup>[99]</sup> a 3D laser-induced graphene (LIG) foam printing process was created based on laminated item manufacture, an extensively used 3D printing approach. Figure 12(a) illustrates the 3D LIG foams fabricated by preparing layers of LIG via irradiating polyimide (PI) film. The prominent 2D peaks and high D/G ratios in the Raman spectra morphologies indicate that graphene has defects (Figure 12b). Because of its electrical and mechanical quantities, 3D LIG is a promising candidate in energy storage applications. To provide evidence, 3D LIG was evaluated as electrodes in Li-ion hybrid supercapacitors (LIHMSCs). The GCD curves of the LIHMSCs from 3D LIG foams are shown in Figure 12(c) at various current densities ranging from 0.01 to 4.2 V. These curves display a strong linear relation at higher current densities, which can be interpreted as superior power performance. The cell could

deliver 970 W/kg of specific power and 64 Wh/kg of specific energy, all of which are based on 100% of the weight of both electrodes. The LIHMSCs cell can support long-range cycling, as illustrated in Figure 12(d). After 970 cycles at 0.1 A/g, there is a retention of around 70% of the specific energy. LIHMSCs are still in their infancy in micro-device production because of their complicated techniques and high costs.

In their study, Shao et al.<sup>[100]</sup> employed electrohydrodynamics to create 3D crumpled MoS<sub>2</sub> (c-MoS<sub>2</sub>) and a stable ink without additives for scalable IJP. The IJP production method for 3D 1T c-MoS<sub>2</sub>/rGO interdigital patterns is illustrated in Figure 12(e). The researchers also conducted density functional theory (DFT) calculations within a computational hydrogen electrode model to investigate the hydrogen evolution reaction (HER) behavior of defective MoS<sub>2</sub> in the presence of different cation electrolytes, as shown in Figure 12(f). The calculations were used to determine the hydrogen adsorption-free energy (GH) for a variety of cations. It was found that the HER is catalyzed at the defect sites of the MoS<sub>2</sub> surface under low overpotential. Compared with the intrinsic 1T distorted basal plane, GH increases dramatically when more metal cations are introduced, as the adsorbed metal ions become fixed on the active sites. When the divalent cation Mg<sup>2+</sup> stays on the flawed basal plane of 1T MoS<sub>2</sub>, GH grows with larger metal cation radii until it stabilizes at around 0.8 eV. Optical microscopy (Figure 12g) reveals the precise printing of two individually identifiable and thoughtfully designed interdigital electrodes. With the large extended stable working voltage of 1.75 V for a single device in MgSO<sub>4</sub>-based aqueous electrolyte, the 3D 1T c-

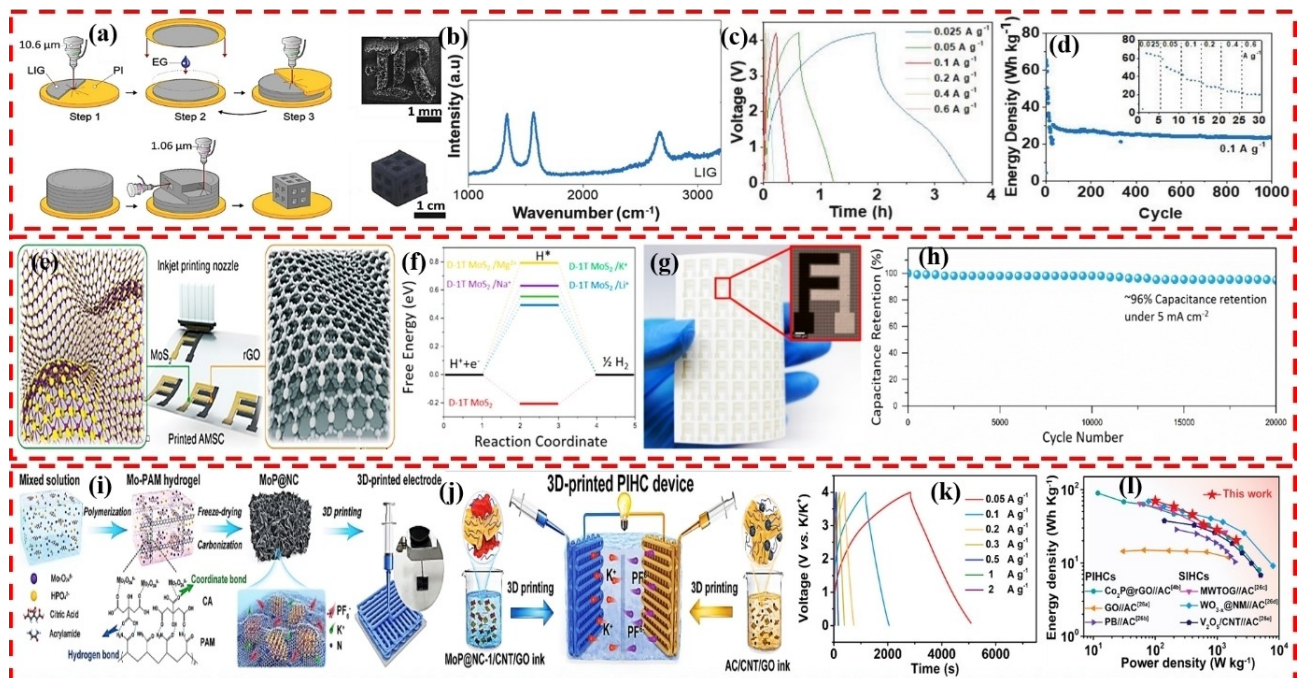


**Figure 12.** a) LOM method 3D-LIG and graphene foams, b) Raman spectrum, c) GCD curves of 3D-LIG cell LIHMSCs, d) cycling stability. Reproduced with permission from Ref. [99]. Copyright (2018) Wiley. e) Schematic depiction of the IJP Mg-ion hybrid MSC comprising 3D 1T c-MoS<sub>2</sub> (left) and rGO (right), f) HER reaction coordinate versus free energy, g) optical micrograph of MSC, h) cycling stability. Reproduced with permission from Ref. [100]. Copyright (2018) American Chemical Society. i) Schematic of MoP@NC and 3D printed electrode synthesis (inset at the top-right corner), j) schematic diagram of MoP@NC//AC charging device, k) GCD curves, l) Ragone plot. Reproduced with permission from Ref. [101]. Copyright (2021) Wiley.

$\text{MoS}_2/\text{rGO}$  can be achieved a high areal specific energy of  $3.85 \text{ Wh/cm}^2$  and a maximum specific power of  $12.6 \text{ mW/cm}^2$ . The device's cycle stability was tested by the GCD at  $5 \text{ mA/cm}^2$ , demonstrating that the capacitance was still 96% of the initial capacitance after 20,000 cycles (Figure 12h).

Zong et al.<sup>[101]</sup> demonstrated the synthesis of MoP nanoparticles on nitrogen-doped carbon nanosheets (MoP@NC), as shown in Figure 12(i). The researchers also explored 3D printing as a promising method for rapidly fabricating complex mechanical and electrical system prototypes, specifically potassium-ion hybrid micro-supercapacitors (PIHMSCs). To create the PIHMSCs, conductive MoP@NC-1/CNT/GO ink and AC/CNT/GO ink were formulated by combining active materials (MoP@NC-1 or AC) with GO and CNT additives at a specific mass ratio. Then, PIHMSCs with a voltaic potential range of  $0.01\text{--}0.4 \text{ V}$  were constructed using a 3D-printed MoP@NC-1 anode and an AC cathode, as shown in Figure 12(j). The GCD curves, as demonstrated in Figure 12(k), have a triangular shape up to  $2 \text{ A/g}$ , indicating that capacitive behavior predominates in the energy storage process of MoP@NC/AC. The PIHMSCs also achieved a high specific energy of  $69.7 \text{ Wh/kg}$ , with a corresponding specific power of  $2041.6 \text{ W/kg}$  (Figure 12l). These results highlighted the high specific energy/power and wide potential range of the PIHMSCs, demonstrating that the proposed 3D-printed electrode design is well-suited for potential applications in the future.

The 3D printing techniques, namely Binder jetting (BJT) and Laminated Object Manufacturing (LOM), utilized for fabricating electrode materials for MIHSCs exhibit some advantages and disadvantages. The BJT technique offers customization according to specific electrode requirements, high throughput, and cost-effectiveness due to its ability to process materials on a large scale and its efficient material utilization. Additionally, lower resolution, limited conductivity, and complex post-processing lead to inconsistent electrochemical performance and lower cyclic stabilities. The LOM technique allows for easy scalability in producing a large number of electrodes with high precision, and versatility in material selection, including con-

ductive polymers and composites, thereby enabling customization to suit specific electrode requirements of the fabrication of microelectrochemical devices. Despite these benefits, LOM does have some drawbacks, such as limitations in complexity, challenges with layer adhesion, and relatively lower conductivity. Table 1 shows representative reports in recent years on various 3D printed techniques based on resolution, costing materials, strength, and weakness for electrodes in different types of MSCs, MBs, and MIHMSCs.

In summary, despite their outstanding performance, MIHMSCs are still in the early stages of development in the field of micro-device manufacturing due to their complex methods and high costs. However, using the benefits of MB's exceptional specific energy and MSCs' exceptional specific power and cycle stability is considered a promising new area of study for micro-energy storage devices. Table 2 lists representative reports in recent years on the application of 3D-printed electrodes in different types of MSCs, MBs, and MIHMSCs.

#### 4. Conclusion and Future Perspective

In conclusion, 3D-printing plays a significant role in the micro-fabrication of MEESDs by making the process more straightforward and repeatable and providing portable and integrative features as compared to traditional approaches. This review provides a brief overview of the fundamentals of essential materials for electrodes, electrolytes, current collectors, and the materials in packaging. Additionally, we conducted an in-depth analysis of specific techniques of 3D-printing process involved in fabrication and the applications of 3D printing techniques on various MEESDs such as MBs, MSCs, and MIHMSCs. Additionally, we discussed the difficulties researchers faced in this area and the potential directions and prospects for future research and development.

3D printing technique enables the rapid and precise fabrication of complex, free-form configurations. These structures can be adjusted in terms of thickness, inter-structural

**Table 1.** Comparison summary of various 3D printed (MEESDs) techniques.

Printing techniques	Resolution	Costing materials	Strengths	Weaknesses
Inkjet printing (IJP)	Micrometers	Conductive polymers, and carbon-based materials	Fast prototyping, digital pattern customization, high throughput, high precision, scalable, flexible, high uniformity and reproducibility, little material waste, non-contact, mask-free	Expensive equipment, High requirements for ink, nozzles prone to clogging
Direct ink writing (DIW)	Micrometers	Plastics, metals, ceramics, and composites	Affordable cost, easy operation, wide material diversity, and no mask requirement	Stringent requirements for ink
Fused deposition modelling (FDM)	Micrometers	Thermoplastic filaments	User-friendliness, low cost, high speed, large size capability, and lack of chemical post-processing requirement	Limited resolution, weak mechanical properties, high viscosity of the molten materials, and low surface quality
Stereolithography (SLA)	Micrometers	Photopolymers	High resolution, high surface finish, and high efficiency	Severe limitation in multi-material deposition
Electrodeposition (ED)	Micrometers	Metals	High accuracy	Limited to metals, complex setup
Laminated Object Manufacturing (LOM)	Micrometers	Paper, Plastic	Fast printing	Limited resolution, material limitations

**Table 2.** Summary and comparison of representative 3D printed (MEESDs), using different materials and techniques.

Device system	Electrodes	Electrolytes	Printing technique	Configuration	Electrochemical performance	Ref.
EDCL	Graphene-GNP aerogel	LiOH/PVA gel	DIW	Sandwiched	4.76 F/g (at 0.4 A/g), 95.5 % after 10000 cycles	[102]
EDCL	Ti <sub>3</sub> C <sub>2</sub> T <sub>x</sub>	PVA/H <sub>2</sub> SO <sup>4-</sup>	3D printing	Interdigital	1035 mF/cm <sup>2</sup> , 51.7 µWh/cm <sup>2</sup> , 1200 cycles (90%)	[103]
EDCL	Graphene/ MWNT	KOH	DIW	Sandwiched	639.56 mF/cm <sup>2</sup> (at 4 mA/cm <sup>2</sup> ), 90 % after 10 000 cycles	[104]
PCSc	PANI/rGO	H <sub>2</sub> SO <sup>4-</sup> /PVA gel	DIW	Interdigitated	1329 mF/cm <sup>2</sup> (at 4.2 mA/cm <sup>2</sup> ), 75 % after 1000 cycles	[105]
PCSc	GO/PANI/PEDOT: PSS	H <sub>2</sub> SO <sup>4-</sup> /PVA gel	DIW	Interdigitated	37.8 F/cm <sup>2</sup> (at 5 mV/s), 75 % after 5000 cycles	[32]
PCSc	MoO <sub>3</sub> /rGO	H <sub>2</sub> SO <sup>4-</sup> /PVA gel	IJP	Interdigital	22.5 F/ cm <sup>3</sup> (1 A/cm <sup>3</sup> ), 82 % over 10 000 cycles	[106]
Li-ion battery	Anode: LTO Cathode: LFP	LiClO <sub>4</sub>	DIW	Interdigitated	1.2 mAh/cm <sup>2</sup> (at 0.5 C), 9.7 J/cm <sup>2</sup> , 2.7 mW/ cm <sup>2</sup>	[66]
Li-ion battery	Cathode: MWCNT	Polysulfide catholyte	IJP	Half	1260 mAh/g (at C/2), 800 mAh/g for 100 cycles (at C/2 and sulfur loading of 3.4 mg S/cm <sup>2</sup> )	[107]
Li-air-battery	Cathode: Co-NC	LiClO <sub>4</sub> -DMSO	DIW	Half	Energy density of 798 Wh/kg cell	[88]
Li-ion S-battery	Cathode: Sulfur copolymer-graphene	LiTFSI	DIW	Half	812.8 mAh/g (at 50 mA/g), 43.4 % after 50 cycles	[108]
Zn–Ag battery	Anode: Zn Cathode: Ag <sub>2</sub> O	KOH/ZnO	IJP	Sandwiched	300 Wh/kg, 600 W/kg	[109]
Zn-Air-battery	Anode: Zn Cathode: rGO/MnO <sub>2</sub> /CNT	PVA/ [BMIM] (OH)	DIW	Interdigitated	142.8 Ah/cm (at 0.1 mA/cm <sup>2</sup> ),	[110]
Na-ion-battery	Anode: MoS <sub>2</sub> -rGO aero-gel	NaClO <sub>4</sub>	IJP	Sandwiched	From 800 mAh/g to 429 mAh/g (in first 10 cycles at 100 mA/g)	[111]

spacing, and finger width, resulting in a porous channel with a lower tortuosity and increased effective area. This enhances the specific energy and specific power of the device. DIW, a common technique within 3D printing, is frequently utilized to print electrodes and other components for various types of MEESDs. This is because DIW inks are similar to the slurries used in traditional manufacturing. However, the printing method, which is done layer-by-layer, still places constraints on the design of printable structures. IJP is an additional 3D printing technology that is extensively applied in micro-energy storage devices. Using this method, it is possible to print electrodes with a variety of planar designs, current collectors/substrates, and electrolyte/separators. However, its uses in a 3D configuration are limited because the ink has high fluidity, and the layer stacking process is sluggish. The use of FDM for printing planar structures of LIBs and SCs, as well as for constructing current collectors, substrates, and various types of packages, has been growing in recent years. However, FDM still faces challenges, including the form of the deposited droplets and the high production cost associated with reducing nozzle diameter. Additionally, FDM components have low precision and resolution, and many thermoplastic materials have low electrical conductivity. SLA is often used to print substrates for electrodepositing electrodes through post-processing or to print other components directly due to the poor electrochemical performance of large volumes of photocurable material in the feedstock. While traditional SLA has low resolution, more recent methods such as DLP and sheet lamination process (SLP) can achieve higher levels of detail. However, factors such as printing speed, resolution, and production cost should be considered when using SLA in

MEMS. Similarly, SLM and selective laser sintering(SLS) are mainly used for printing current collectors and substrates for electrodes, but face challenges, including high production cost and uneven finished product quality. LOM and BJJG have also been employed for printing electrodes or electrolytes in MEESDs, but drawbacks include high anisotropy in LOM and low mechanical strength in BJJG, as well as the need for extensive post-treatment. DED, used only for repairing or adding specific material parts to improve existing components, is rarely used in MEESDs due to its low resolution, rough final surface, and inability to construct complex 3D structures thicker than 3D. Despite tremendous advancements in recent years, 3D printing technologies still face substantial challenges that should be addressed to enable them for practical applications.

(1) Choice of Ink-preparation in 3D printing (Figure 13a). The commercial success of 3D printing technologies in energy storage devices, such as batteries and SCs, will depend on developing low-cost, high-performance methods for preparing inks and filaments from functional materials. It is recommended to print active materials directly, without using polymeric binders or thermoplastic polymer additives to maximize electrochemical performance. The preparation of inks and filaments must consider various requirements of the active material powders, including particle size, surface chemistry, hydrophilicity, miscibility, and density. Large-scale production of high-quality material powders with the desired properties is crucial for the effective use of 3D-printed devices. However, one limitation of printed electrodes is that they often lack mechanical robustness, which can lead to cracking during assembly. Further study is required to enhance the mechanical properties of 3D-

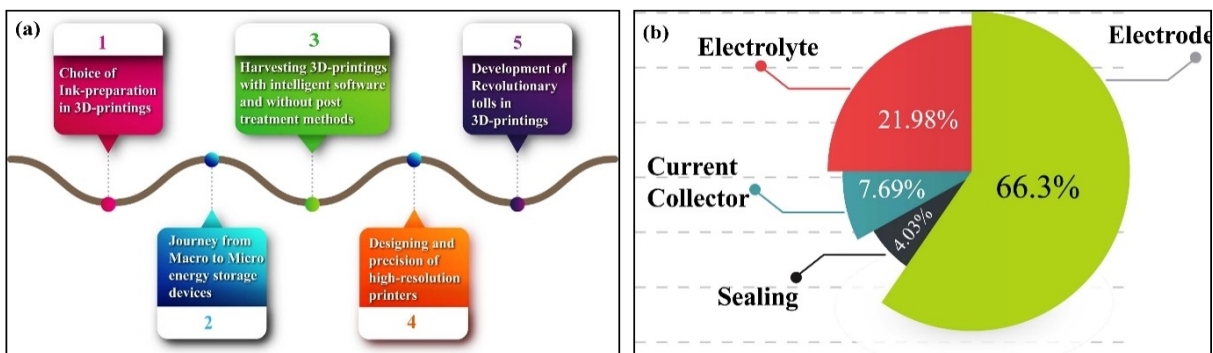


**Figure 13.** a) Future perspective for 3D printing in energy storage applications. b) Percentage related to developing each component (electrode, electrolyte, current collector, and sealing) for 3D printing techniques for MEESDs.

printed electrodes without compromising their superior electrochemical performance. This can be achieved by optimizing printing techniques and active materials to achieve aligned structures or by reevaluating post-printing treatment processes and starting materials, such as thermal sintering or adding reinforcement additives.

- (2) The journey from macro to micro energy storage devices (Figure 13a). Currently, the 3D printed components only provide macroscale porous structures. However, new printing techniques such as electrospray, EHD printing, and two-photon polymerization (2PP) have the potential to achieve hierarchical porous structures with pore sizes ranging from macro to micro, thereby obtaining improved resolution of the equipment and enhanced electrochemical performance. Fully continuous or one-step printing is also a promising direction for future development. By expanding the versatility of 3D printing techniques, it is possible to create customized self-powered devices while easing the requirements for feedstock materials with specific intrinsic properties and physical characteristics. Additionally, the compatibility between different 3D printing techniques could simplify technical processes and reduce operating costs.
- (3) Harvesting 3D printing with intelligent software and without post-treatment methods: While the process of 3D printing seems simple, many complex factors affect the repeatability of printed parts based on the same CAD model, and post-treatment processes. There is a need for more advanced software, control systems, high-quality industrial equipment, and methods that do not require post-treatment. Additionally, 3D printing has the potential to facilitate the integration of printed devices with other electrical elements, enabling the creation of lightweight, miniaturized devices and reducing fabrication costs in terms of time, energy, and money. There is a trend toward developing self-powered energy systems that combine a harvester and a battery to compensate for the low energy density of MEESDs while providing continuous power to other electronic devices.
- (4) Designing and precision of high-resolution printers (Figure 13a). There is an ongoing challenge in improving the

precision of printers for use in the design and application of MEESDs. While most printers can print materials at the microscale, they cannot print functional materials at the nanoscale, which enables the control of ion migration. While these processes can be controlled to some extent, they do not provide complete control. The diameter of the powdered materials in functional material printing is also a major limiting factor in terms of resolution. To enhance the application of 3D printing in the development of MBs and SCs, it is crucial to develop high-resolution printers and formulate functional inks that are compatible with these advanced printing systems.

- (5) Development of revolutionary tools in 3D printings (Figure 13a). Electrode materials are crucial for achieving high-performance electrochemical energy storage devices. Software design and simulation are essential for designing novel, efficient advanced electrode structures.<sup>[112]</sup> Recently, many electrode geometries have been designed using human intuition rather than scientific theoretical calculations. The advancement of machine learning algorithms will enable the automatic design and optimization of more complex electrode architectures, saving time and making electrode architecture design more effective.<sup>[113]</sup> As a transformative tool, 3D printing can be used to address fundamental issues related to energy storage devices, and it can also be used to design and manufacture high-performance electrodes. The rapidly developing additive manufacturing technology of 4D printing has also gained attention. Using this technique, 3D printed devices can evolve or reconfigure their architectures over time in response to changes in external environmental factors, spontaneously adjusting their physicochemical properties. This process is expected to no longer require manual operation, further improving the durability and performance of printed MESDs and enabling the development of smart electrochemical energy storage solutions. 3D printing technology has made significant advancements in various fields and has a promising future. Although the application of 3D printing techniques for energy storage has grown rapidly in recent years, related research is still in its early stages. Further research is required to explore its commer-

- cial and practical applications. Soon, we anticipate further exciting and significant advancements in using 3D printing technologies for energy storage.
- (6) In our study, we have emphasized the contributions of 3D printing techniques in energy storage devices and the percentage related to developing each component, such as electrodes, electrolytes, current collectors, and sealing in Figure 13(b). By providing a comprehensive understanding of these contributions, our research is a valuable resource for guiding future research directions. This information can help researchers identify areas with potential for improvement, optimize the use of 3D printing techniques, and ultimately advance the development of more efficient and sustainable energy storage solutions.

## Acknowledgements

This research was conducted in collaboration with Shanghai Enli Power Technology Co., Ltd., and Beijing Enli Power Technology Co., Ltd. This study was also partly supported by a Hubei Provincial High-level Innovative Talent Program (No. 2021HG01) from Hubei province, China; a Pearl Scholars Research (No. P20190128, P20190129), and a Young Scholars Start-up Research (No. Y20190128, Y20190129) from Huanggang Normal University, Hubei province, China.

## Conflict of Interests

The authors declare no conflict of interest.

## Data Availability Statement

The data that support the findings of this study are available on request from the corresponding author. The data are not publicly available due to privacy or ethical restrictions.

**Keywords:** 3D printing • additive manufacturing • micro-supercapacitors • metal-ion hybrid micro-supercapacitors • micro-batteries

- [1] a) J. Schot, L. Kanger, G. J. N. e. Verbong, *Nat. Energy* **2016**, *1*, 1–7; b) M. Cheng, R. Deivanayagam, R. J. B. Shahbazian-Yassar, *Batteries & Supercaps* **2020**, *3*, 130–146.
- [2] X. Y. Yu, X. W. J. A. E. M. Lou, *Adv. Energy Mater.* **2018**, *8*, 1701592.
- [3] a) M. S. Javed, A. Mateen, S. Ali, X. Zhang, I. Hussain, M. Imran, S. S. A. Shah, W. J. S. Han, *Small* **2022**, *01*, 989; b) M. S. Javed, A. Mateen, I. Hussain, S. Ali, S. Asim, A. Ahmad, E. tag Eldin, M. A. Bajaber, T. Najam, W. J. C. E. J. Han, *J. Chem. Eng.* **2022**, *452*, 139455; c) M. S. Javed, A. Mateen, I. Hussain, A. Ahmad, M. Mubashir, S. Khan, M. A. Assiri, S. M. Eldin, S. S. A. Shah, W. J. E. S. M. Han, *Energy Storage Mater.* **2022**, *53*, 827–872.
- [4] a) A. Polman, M. Knight, E. C. Garnett, B. Ehrler, W. C. J. S. Sinke, *Science* **2016**, *352*, aad4424; b) M. F. El-Kady, Y. Shao, R. B. J. N. R. M. Kaner, *Nat. Rev. Mater.* **2016**, *1*, 1–14.
- [5] X. Xu, Y. H. Tan, J. Ding, C. J. E. Guan, *Energy Environ. Mater.* **2022**, *5*, 427–438.

- [6] a) W. A. Haider, L. He, H. A. Mirza, M. Tahir, A. M. Khan, K. A. Owusu, W. Yang, Z. Wang, L. J. R. a. Mai, *RSC Adv.* **2020**, *10*, 18245–18251; b) Z. Zhu, R. Kan, S. Hu, L. He, X. Hong, H. Tang, W. J. S. Luo, *Small* **2020**, *16*, 2003251; c) M. Tahir, L. He, W. Yang, X. Hong, W. A. Haider, H. Tang, Z. Zhu, K. A. Owusu, L. J. J. o. E. C. Mai, *J. Energy Chem.* **2020**, *49*, 224–232; d) W. Yang, Y. Zhu, Z. Jia, L. He, L. Xu, J. Meng, M. Tahir, Z. Zhou, X. Wang, L. J. A. E. M. Mai, *Adv. Energy Mater.* **2020**, *10*, 2001873.
- [7] a) A. Selimis, V. Mironov, M. J. M. E. Farsari, *Microelectron. Eng.* **2015**, *132*, 83–89; b) B. J. B. h. Berman, *Bus. Horiz.* **2012**, *55*, 155–162.
- [8] J.-Y. Lee, J. An, C. K. J. A. m. t. Chua, *App Mater.Today.* **2017**, *7*, 120–133.
- [9] a) W. A. Haider, M. Tahir, L. He, H. Mirza, R. Zhu, Y. Han, L. J. A. C. S. Mai, *ACS Cent. Sci.* **2020**, *6*, 1901–1915; b) X. Ma, X. Hong, L. He, L. Xu, Y. Zhang, Z. Zhu, X. Pan, J. Zhu, L. J. A. a. m. Mai, *ACS Appl. Mater. Interfaces* **2018**, *11*, 948–956; c) C. Yin, L. He, Y. Wang, Z. Liu, G. Zhang, K. Zhao, C. Tang, M. Yan, Y. Han, L. J. R. a. Mai, *RSC Adv.* **2016**, *6*, 43436–43441.
- [10] a) M. Tahir, L. Li, L. He, Z. Xiang, Z. Ma, W. A. Haider, X. Liao, Y. J. E. Song, *Energy Environ. Mater.* **2022**, e12546; b) Y. Duan, G. You, K. Sun, Z. Zhu, X. Liao, L. Lv, H. Tang, B. Xu, L. J. N. A. He, *Nanoscale Adv.* **2021**, *3*, 6271–6293; c) X. Hong, X. Ma, L. He, Y. Dai, X. Pan, J. Zhu, W. Luo, Y. Su, L. J. S. Mai, *Small* **2021**, *17*, 2007791; d) Z. Zhu, R. Kan, P. Wu, Y. Ma, Z. Wang, R. Yu, X. Liao, J. Wu, L. He, S. J. S. Hu, *Small* **2021**, *17*, 2103136.
- [11] X. Wang, M. Jiang, Z. Zhou, J. Gou, D. Hui, *Compos. B. Eng.* **2017**, *110*, 442–458.
- [12] A. Vyatskikh, S. Delalande, A. Kudo, X. Zhang, C. M. Portela, J. R. Greer, *Nat. Commun.* **2018**, *9*, 1–8.
- [13] R. Trombetta, J. A. Inzana, E. M. Schwarz, S. L. Kates, H. Awad, *Ann. Biomed. Eng.* **2017**, *45*, 23–44.
- [14] H. N. Chia, B. Wu, *J. Biol. Eng.* **2015**, *9*, 1–14.
- [15] J. A. Inzana, D. Olvera, S. M. Fuller, J. P. Kelly, O. A. Graeve, E. M. Schwarz, S. L. Kates, H. Awad, *Biomaterials* **2014**, *35*, 4026–4034.
- [16] A. D. Valentine, T. A. Busbee, J. W. Boley, J. R. Raney, A. Chortos, A. Kotikian, J. D. Berrigan, M. F. Durstock, J. Lewis, *Adv. Mater.* **2017**, *29*, 1703817.
- [17] C. Gosselin, R. Duballet, P. Roux, N. Gaudilliére, J. Dirrenberger, P. J. M. Morel, *Mater. Des.* **2016**, *100*, 102–109.
- [18] S. V. Murphy, A. J. N. b. Atala, *Nat. Biotechnol.* **2014**, *32*, 773–785.
- [19] X. Tian, J. Jin, S. Yuan, C. K. Chua, S. B. Tor, K. J. A. E. M. Zhou, *Adv. Energy Mater.* **2017**, *7*, 1700127.
- [20] a) X. Gao, X. Yang, Q. Sun, J. Luo, J. Liang, W. Li, J. Wang, S. Wang, M. Li, R. J. E. S. M. Li, *Energy Storage Mater.* **2020**, *24*, 682–688; b) A. Sajedi-Moghaddam, E. Rahamanian, N. J. A. a. m. Naseri, *ACS Appl. Mater. Interfaces* **2020**, *12*, 34487–34504.
- [21] A. T. Kutbee, R. R. Bahabry, K. O. Alamoudi, M. T. Ghoneim, M. D. Cordero, A. S. Almuslem, A. Gumus, E. M. Diallo, J. M. Nassar, A. M. J. n. f. e. Hussain, *npj flexible Electron.* **2017**, *1*, 1–8.
- [22] X. Tian, K. J. N. Zhou, *Nanoscale* **2020**, *12*, 7416–7432.
- [23] J. Huang, J. Yang, W. Li, W. Cai, Z. J. T. S. F. Jiang, *Thin Solid Films* **2008**, *516*, 3314–3319.
- [24] Y. Wang, C. Chen, H. Xie, T. Gao, Y. Yao, G. Pastel, X. Han, Y. Li, J. Zhao, K. J. A. F. M. Fu, *Adv. Funct. Mater.* **2017**, *27*, 1703140.
- [25] K. Fu, Y. Wang, C. Yan, Y. Yao, Y. Chen, J. Dai, S. Lacey, Y. Wang, J. Wan, T. J. A. M. Li, *Adv. Mater.* **2016**, *28*, 2587–2594.
- [26] X. Lu, T. Zhao, X. Ji, J. Hu, T. Li, X. Lin, W. J. J. o. A. Huang, *Compounds, J. Alloys Compd.* **2018**, *760*, 78–83.
- [27] J. Hu, Y. Jiang, S. Cui, Y. Duan, T. Liu, H. Guo, L. Lin, Y. Lin, J. Zheng, K. J. A. E. M. Amine, *Adv. Energy Mater.* **2016**, *6*, 1600856.
- [28] S. D. Lacey, D. J. Kirsch, Y. Li, J. T. Morgenstern, B. C. Zarket, Y. Yao, J. Dai, L. Q. Garcia, B. Liu, T. Gao, *Adv. Mater.* **2018**, *30*, 1705651.
- [29] S. Lin, Y. Zhong, X. Zhao, T. Sawada, X. Li, W. Lei, M. Wang, T. Serizawa, H. Zhu, *Adv. Mater.* **2018**, *30*, 1803004.
- [30] D. Cao, Y. Xing, K. Tantratian, X. Wang, Y. Ma, A. Mukhopadhyay, Z. Cheng, Q. Zhang, Y. Jiao, L. Chen, *Adv. Mater.* **2019**, *31*, 1807313.
- [31] J. H. Kim, S. Lee, M. Wajahat, H. Jeong, W. S. Chang, H. J. Jeong, J.-R. Yang, J. T. Kim, S. Seol, *ACS Nano* **2016**, *10*, 8879–8887.
- [32] Y. Liu, B. Zhang, Q. Xu, Y. Hou, S. Seyedin, S. Qin, G. G. Wallace, S. Beirne, J. M. Razal, J. J. A. F. M. Chen, *Adv. Funct. Mater.* **2018**, *28*, 1706592.
- [33] P. Sundriyal, S. Bhattacharya, *ACS Appl. Energ. Mater.* **2019**, *2*, 1876–1890.
- [34] Z. Xu, C. Fan, Q. Zhang, Y. Liu, C. Cui, B. Liu, T. Wu, X. Zhang, W. Liu, *Adv. Funct. Mater.* **2021**, *31*, 2100462.

- [35] B. Yiming, Y. Han, Z. Han, X. Zhang, Y. Li, W. Lian, M. Zhang, J. Yin, T. Sun, Z. Wu, *Adv. Mater.* **2021**, *33*, 2006111.
- [36] S.-H. Kim, K.-H. Choi, S.-J. Cho, J. Yoo, S.-S. Lee, S.-Y. Lee, E. Science, *Energy Environ. Sci.* **2018**, *11*, 321–330.
- [37] P. Sundriyal, S. Bhattacharya, *ACS Appl. Energ. Mater.* **2019**, *2*, 1876–1890.
- [38] D. W. McOwen, S. Xu, Y. Gong, Y. Wen, G. L. Godbey, J. E. Gritton, T. R. Hamann, J. Dai, G. T. Hitz, L. Hu, E. D. Wachsman, *Adv. Mater.* **2018**, *30*, 1707132.
- [39] S. Zekoll, C. Marriner-Edwards, A. O. Hekselman, J. Kasemchainan, C. Kuss, D. E. Armstrong, D. Cai, R. J. Wallace, F. H. Richter, J. Thijssen, *Energy Environ. Sci.* **2018**, *11*, 185–201.
- [40] C. Chae, J. H. Han, S. S. Lee, Y. Choi, T. H. Kim, S. Jeong, *Adv. Funct. Mater.* **2020**, *30*, 2000715.
- [41] L. Liu, Q. Lu, S. Yang, J. Guo, Q. Tian, W. Yao, Z. Guo, V. A. Roy, W. Wu, *Adv. Mater. Technol.* **2018**, *3*, 1700206.
- [42] B. Xie, Y. Wang, W. Lai, W. Lin, Z. Lin, Z. Zhang, P. Zou, Y. Xu, S. Zhou, C. J. N. E. Yang, *Nano Energy* **2016**, *26*, 276–285.
- [43] B. Chen, Y. Jiang, X. Tang, Y. Pan, S. Hu, *ACS Appl. Mater. Interfaces* **2017**, *9*, 28433–28440.
- [44] a) P. Simon, Y. Gogotsi, *Nanoscience and Technology: a Collection of Reviews from Nature Journals*, World Scientific, **2010**, pp. 320–329; b) V. Augustyn, P. Simon, B. J. E. Dunn, *E. S. Energy Environ. Sci.* **2014**, *7*, 1597–1614; c) V. Augustyn, J. Come, M. A. Lowe, J. W. Kim, P.-L. Taberna, S. H. Tolbert, H. D. Abruna, P. Simon, B. Dunn, *Nat. Mater.* **2013**, *12*, 518–522; d) M. S. Javed, A. Mateen, I. Hussain, A. Ahmad, M. Mubashir, S. Khan, M. A. Assiri, S. M. Eldin, S. Shah, W. Han, *Energy Storage Mater.* **2022**, *53*, 827–872; e) A. Mateen, M. S. Javed, S. Khan, A. Saleem, M. K. Majeed, A. J. Khan, M. F. Tahir, M. A. Ahmad, M. A. Assiri, K.-Q. Peng, *J. Energy Storage* **2022**, *49*, 104150.
- [45] a) J.-G. Wang, F. Kang, B. Wei, *Prog. Mater. Sci.* **2015**, *74*, 51–124; b) Q. Abbas, A. Mateen, S. H. Siyal, N. U. Hassan, A. A. Alothman, M. Ouladsmane, S. M. Eldin, M. Z. Ansari, M. S. Javed, *Chemosphere* **2023**, *313*, 137421; c) A. Sajedi-Moghaddam, M. Gholami, N. J. A. M. Naseri, *ACS Appl. Mater. Interfaces* **2023**, *15*, 3894–3903.
- [46] H. Y. Lee, J. B. J. o. S. S. C. Goodenough, *J. Solid State Chem.* **1999**, *144*, 220–223.
- [47] Y. He, W. Chen, X. Li, Z. Zhang, J. Fu, C. Zhao, E. Xie, *ACS Nano* **2013**, *7*, 174–182.
- [48] B. Yao, S. Chandrasekaran, J. Zhang, W. Xiao, F. Qian, C. Zhu, E. B. Duoss, C. M. Spadaccini, M. A. Worsley, Y. Li, *Joule* **2019**, *3*, 459–470.
- [49] K. Shen, J. Ding, S. J. A. E. M. Yang, *Adv. Energy Mater.* **2018**, *8*, 1800408.
- [50] S. E. Moosavifard, J. Shamsi, M. K. Altafi, Z. Moosavifard, *Chem. Commun.* **2016**, *52*, 13140–13143.
- [51] X. Li, H. Li, X. Fan, X. Shi, J. Liang, *Adv. Energy Mater.* **2020**, *10*, 1903794.
- [52] Z. Yang, X. Yang, T. Yang, Y. Cao, C. Zhang, Y. Zhang, P. Li, J. Yang, Y. Ma, Q. Li, *Energy Storage Mater.* **2023**, *54*, 51–59.
- [53] a) T. S. Wei, B. Y. Ahn, J. Grotto, J. Lewis, *Adv. Mater.* **2018**, *30*, 1703027; b) J. Zhao, Y. Zhang, Y. Huang, J. Xie, X. Zhao, C. Li, J. Qu, Q. Zhang, J. Sun, B. J. A. S. He, *Adv. Sci.* **2018**, *5*, 1801114; c) H. Pang, Y. Zhang, W.-Y. Lai, Z. Hu, W. Huang, *Nano Energy* **2015**, *15*, 303–312.
- [54] a) A. G. Pandolfo, A. Hollenkamp, *J. Power Sources* **2006**, *157*, 11–27; b) L. L. Zhang, X. Zhao, *Chem. Soc. Rev.* **2009**, *38*, 2520–2531; c) E. Frackowiak, *Phys. Chem. Chem. Phys.* **2007**, *9*, 1774–1785.
- [55] K. Novoselov, V. Fal, *Nature* **2012**, *490*, 192–200.
- [56] K. Fu, Y. Yao, J. Dai, L. Hu, *Adv. Mater.* **2017**, *29*, 1603486.
- [57] J. J. Shao, W. Lv, Q. Yang, *Adv. Mater.* **2014**, *26*, 5586–5612.
- [58] G. Sun, J. An, C. K. Chua, H. Pang, J. Zhang, P. Chen, *Electrochim. Commun.* **2015**, *51*, 33–36.
- [59] S. Tagliaferri, G. Nagaraju, A. Panagiotopoulos, M. Och, G. Cheng, F. Iacoviello, C. Mattevi, *ACS Nano* **2021**, *15*, 15342–15353.
- [60] S. Yuan, W. Fan, D. Wang, L. Zhang, Y.-E. Miao, F. Lai, T. Liu, *J. Mater. Chem.* **2021**, *9*, 423–432.
- [61] C. Zhu, T. Liu, F. Qian, T. Y.-J. Han, E. B. Duoss, J. D. Kuntz, C. M. Spadaccini, M. A. Worsley, Y. Li, *Nano Lett.* **2016**, *16*, 3448–3456.
- [62] A.-K. Lu, H.-Y. Li, Y. Yu, *J. Mater. Chem.* **2019**, *7*, 7852–7858.
- [63] a) V. G. Rocha, E. Garcia-Tunon, C. Botas, F. Markoulidis, E. Feilden, E. D'Elia, N. Ni, M. Shaffer, E. Saiz, *ACS Appl. Mater. Interfaces* **2017**, *9*, 37136–37145; b) L. T. Le, M. H. Ervin, H. Qiu, B. E. Fuchs, W. Lee, *Electrochim. Commun.* **2011**, *13*, 355–358; c) T. Nathan-Walleser, I. M. Lazar, M. Fabritius, F. J. Tölle, Q. Xia, B. Bruchmann, S. S. Venkataraman, M. G. Schwab, R. Mühlaupt, *Adv. Funct. Mater.* **2014**, *24*, 4706–4716; d) H. Jung, C. Ve Cheah, N. Jeong, J. Lee, *Appl. Phys. Lett.* **2014**, *105*, 053902; e) M. H. Ervin, L. T. Le, W. Lee, *Electrochim. Acta* **2014**, *147*, 610–616.
- [64] a) X.-B. Cheng, R. Zhang, C.-Z. Zhao, Q. Zhang, *Chem. Rev.* **2017**, *117*, 10403–10473; b) M. I. Khan, M. Zubair, N. Bibi, F. Aziz, A. Mateen, H. Ali, P. Ahmad, Y. Khan, M. K. Tufail, A. Hassan, *ChemistrySelect* **2021**, *6*, 13301–13308.
- [65] Y. Yang, W. Yuan, X. Zhang, Y. Yuan, C. Wang, Y. Ye, Y. Huang, Z. Qiu, Y. Tang, *Appl. Energy* **2020**, *257*, 114002.
- [66] K. Sun, T. S. Wei, B. Y. Ahn, J. Y. Seo, S. J. Dillon, J. Lewis, *Adv. Mater.* **2013**, *25*, 4539–4543.
- [67] Y. Zhang, S. Zheng, F. Zhou, X. Shi, C. Dong, P. Das, J. Ma, K. Wang, Z. Wu, *Small* **2022**, *18*, 2104506.
- [68] S. Zheng, H. Wang, P. Das, Y. Zhang, Y. Cao, J. Ma, S. Liu, Z. Wu, *Adv. Mater.* **2021**, *33*, 2005449.
- [69] M. Drews, S. Tepner, P. Haberzettl, H. Gentischer, W. Beichel, M. Breitwieser, S. Vierrath, D. Biro, *RSC Adv.* **2020**, *10*, 22440–22448.
- [70] L. Zhou, W. Ning, C. Wu, D. Zhang, W. Wei, J. Ma, C. Li, L. Chen, *Adv. Mater. Technol.* **2019**, *4*, 1800402.
- [71] a) S. Zheng, H. Huang, Y. Dong, S. Wang, F. Zhou, J. Qin, C. Sun, Y. Yu, Z.-S. Wu, X. Bao, *Energy Environ. Sci.* **2020**, *13*, 821–829; b) J. Ma, S. Zheng, P. Das, P. Lu, Y. Yu, Z.-S. Wu, *Small Structures* **2020**, *1*, 2000053; c) H. Li, X. Zhang, Z. Zhao, Z. Hu, X. Liu, G. Yu, *Energy Storage Mater.* **2020**, *26*, 83–104; d) J.-Y. Hwang, S.-T. Myung, Y.-K. Sun, *Chem. Soc. Rev.* **2017**, *46*, 3529–3614.
- [72] J. Ma, S. Zheng, L. Chi, Y. Liu, Y. Zhang, K. Wang, Z. Wu, *Adv. Mater.* **2022**, *34*, 2205569.
- [73] J. Xu, J. Chen, L. Tao, Z. Tian, S. Zhou, N. Zhao, C.-P. Wong, *Nano Energy* **2019**, *60*, 510–519.
- [74] J. Ding, K. Shen, Z. Du, B. Li, S. Yang, *ACS Appl. Mater. Interfaces* **2017**, *9*, 41871–41877.
- [75] D. Ji, H. Zheng, H. Zhang, W. Liu, J. Ding, *J. Alloys Compd.* **2022**, *900*, 163394.
- [76] Z. Lyu, G. J. Lim, J. J. Koh, Y. Li, Y. Ma, J. Ding, J. Wang, Z. Hu, J. Wang, W. Chen, *Joule* **2021**, *5*, 89–114.
- [77] Y. Katsuyama, A. Kudo, H. Kobayashi, J. Han, M. Chen, I. Honma, R. Kaner, *Small* **2022**, *18*, 2202277.
- [78] a) H. Ye, L. Wang, S. Deng, X. Zeng, K. Nie, P. N. Duchesne, B. Wang, S. Liu, J. Zhou, F. Zhao, *Adv. Energy Mater.* **2017**, *7*, 1601602; b) Y. Chen, M. Yousaif, Y. Wang, Z. Wang, S. Lou, R. P. Han, Y. Yang, A. Cao, *Nano Energy* **2020**, *78*, 105265; c) H. Sun, L. Mei, J. Liang, Z. Zhao, C. Lee, H. Fei, M. Ding, J. Lau, M. Li, C. J. S. Wang, *Sci. J.* **2017**, *356*, 599–604; d) F. Shen, W. Luo, J. Dai, Y. Yao, M. Zhu, E. Hitz, Y. Tang, Y. Chen, V. L. Sprinkle, X. Li, *Adv. Energy Mater.* **2016**, *6*, 1600377.
- [79] L. Zolin, M. Chandesris, W. Porcher, B. Lestriez, *Energy Technol.* **2019**, *7*, 1900025.
- [80] M. A. Rahman, X. Wang, C. Wen, *J. Electrochem. Soc.* **2013**, *160*, A1759.
- [81] a) K.-H. Lee, S.-S. Lee, D. B. Ahn, J. Lee, D. Byun, S.-Y. Lee, *Sci. Adv.* **2020**, *6*, eaaz1692; b) F. Xu, T. Wang, W. Li, Z. J. C. p. I. Jiang, *Chem. Phys. Lett.* **2003**, *375*, 247–251; c) J. Zhang, X. L. Li, S. Fan, S. Huang, D. Yan, L. Liu, P. Alvarado, H. Yang, *Mater. Today Energy* **2020**, *16*, 100407.
- [82] K. Jiang, Z. Zhou, X. Wen, Q. Weng, *Small* **2021**, *17*, 2007389.
- [83] H. Ma, X. Tian, J. Fan, W. Cao, X. Yuan, S. Hou, H. Jin, *J. Power Sources* **2022**, *550*, 232152.
- [84] R. Li, L. Li, R. Jia, K. Jiang, G. Shen, D. Chen, *Small Methods* **2020**, *4*, 2000363.
- [85] J. Shi, S. Wang, X. Chen, Z. Chen, X. Du, T. Ni, Q. Wang, L. Ruan, W. Zeng, Z. Huang, *Adv. Energy Mater.* **2019**, *9*, 1901957.
- [86] H. Wang, R. Guo, H. Li, J. Wang, C. Du, X. Wang, Z. Zheng, *J. Chem. Eng.* **2022**, *429*, 132196.
- [87] X. Gao, Q. Sun, X. Yang, J. Liang, A. Koo, W. Li, J. Liang, J. Wang, R. Li, F. Holness, *Nano Energy* **2019**, *56*, 595–603.
- [88] Z. Lyu, G. J. Lim, R. Guo, Z. Kou, T. Wang, C. Guan, J. Ding, W. Chen, J. Wang, *Adv. Funct. Mater.* **2019**, *29*, 1806658.
- [89] a) P. Zhang, Y. Li, G. Wang, F. Wang, S. Yang, F. Zhu, X. Zhuang, O. G. Schmidt, X. Feng, *Adv. Mater.* **2019**, *31*, 1806005; b) P. Zhang, L. Wang, F. Wang, D. Tan, G. Wang, S. Yang, M. Yu, J. Zhang, X. J. B. Feng, *Batteries & Supercaps* **2019**, *2*, 918–923; c) A. Mateen, M. Zubair, M. Saleem, A. Golubenkova, L. Voskressensky, A. A. Alothman, M. Ouladsmane, A. Ahmad, M. Javed, *Energies* **2022**, *15*, 9577; d) A. Mateen, M. Z. Ansari, Q. Abbas, A. Muneeb, A. Hussain, E. T. Eldin, F. M. Alzahrani, N. S. Alsaiari, S. Ali, M. Javed, *Molecules* **2022**, *27*, 7446.
- [90] Z. Fan, C. Wei, L. Yu, Z. Xia, J. Cai, Z. Tian, G. Zou, S. X. Dou, J. Sun, *ACS Nano* **2020**, *14*, 867–876.

- [91] C. Yang, X. Wu, H. Xia, J. Zhou, Y. Wu, R. Yang, G. Zhou, L. Qiu, *ACS Nano* **2022**, *16*, 2699–2710.
- [92] J. Yuan, M. Qiu, J. X. Chen, X. Hu, Y. Liu, B. Yu, G. Zhong, Z. Weng, H. Zhan, Z. Wen, *Adv. Funct. Mater.* **2022**, 2203732.
- [93] a) H. Li, L. Ma, C. Han, Z. Wang, Z. Liu, Z. Tang, C. Zhi, *Nano Energy* **2019**, *62*, 550–587; b) H. Wang, M. Wang, Y. Tang, *Energy Storage Mater.* **2018**, *13*, 1–7.
- [94] a) C. Jiang, Z. Zou, *Diam. Relat. Mater.* **2020**, *101*, 107603; b) Y. Zheng, W. Zhao, D. Jia, Y. Liu, L. Cui, D. Wei, R. Zheng, J. Liu, *J. Chem. Eng.* **2020**, *387*, 124161.
- [95] Z. Fan, J. Jin, C. Li, J. Cai, C. Wei, Y. Shao, G. Zou, J. Sun, *ACS Nano* **2021**, *15*, 3098–3107.
- [96] G. Nagaraju, S. Tagliaferri, A. Panagiotopoulos, M. Och, R. Quintin-Baxendale, C. Mattevi, *J. Mater. Chem.* **2022**, *10*, 15665–15676.
- [97] Y. Liu, S. Zheng, J. Ma, X. Wang, L. Zhang, P. Das, K. Wang, Z. Wu, *Adv. Energy Mater.* **2022**, *12*, 2200341.
- [98] Y. Gu, T. Yu, P. Xue, Q. Zhang, S. Ma, X. Xu, *ChemElectroChem* **2021**, *8*, 4498–4508.
- [99] D. X. Luong, A. K. Subramanian, G. A. L. Silva, J. Yoon, S. Cofer, K. Yang, P. S. Owuor, T. Wang, Z. Wang, J. Lou, *Adv. Mater.* **2018**, *30*, 1707416.
- [100] Y. Shao, J.-H. Fu, Z. Cao, K. Song, R. Sun, Y. Wan, A. Shamim, L. Cavallo, Y. Han, R. Kaner, *ACS Nano* **2020**, *14*, 7308–7318.
- [101] W. Zong, N. Chui, Z. Tian, Y. Li, C. Yang, D. Rao, W. Wang, J. Huang, J. Wang, F. Lai, *Adv. Sci.* **2021**, *8*, 2004142.
- [102] C. Zhu, T. Liu, F. Qian, T. Y.-J. Han, E. B. Duoss, J. D. Kuntz, C. M. Spadaccini, M. A. Worsley, Y. Li, *Nano Lett.* **2016**, *16*, 3448–3456.
- [103] J. Orangi, F. Hamade, V. A. Davis, M. Beidaghi, *ACS Nano* **2019**, *14*, 640–650.
- [104] B. Nan, F. J. Galindo-Rosales, J. Ferreira, *Mater. Today* **2020**, *35*, 16–24.
- [105] Z. Wang, Q. e. Zhang, S. Long, Y. Luo, P. Yu, Z. Tan, J. Bai, B. Qu, Y. Yang, J. Shi, *ACS Appl. Mater. Interfaces* **2018**, *10*, 10437–10444.
- [106] B. Li, N. Hu, Y. Su, Z. Yang, F. Shao, G. Li, C. Zhang, Y. Zhang, *ACS Appl. Mater. Interfaces* **2019**, *11*, 46044–46053.
- [107] C. Milroy, A. Manthiram, *Chem. Commun.* **2016**, *52*, 4282–4285.
- [108] K. Shen, H. Mei, B. Li, J. Ding, S. Yang, *Adv. Energy Mater.* **2018**, *8*, 1701527.
- [109] C. C. Ho, K. Murata, D. A. Steingart, J. W. Evans, P. Wright, *J. Micromech. Microeng.* **2009**, *19*, 094013.
- [110] J. Zhang, X. L. Li, S. Fan, S. Huang, D. Yan, L. Liu, P. Valdivia y Alvarado, H. Y. Yang, *Mater. Today Energy* **2020**, *16*, 100407.
- [111] E. Brown, P. Yan, H. Tekik, A. Elangovan, J. Wang, D. Lin, J. Li, *Mater. Des.* **2019**, *170*, 107689.
- [112] J. Park, J. Li, W. Lu, A. Sastry, *J. Appl. Phys.* **2016**, *119*, 025101.
- [113] T. Zohdi, *Comput. Methods Appl. Mech. Eng.* **2018**, *331*, 343–362.

Manuscript received: May 9, 2023  
 Revised manuscript received: May 28, 2023  
 Accepted manuscript online: May 29, 2023  
 Version of record online: June 21, 2023